Research Square

Preprints are preliminary reports that have not undergone peer review.
They should not be considered conclusive, used to inform clinical practice,
or referenced by the media as validated information.

Vibration and Acoustic Response of Metamaterial Micro-FG Beams Considering Surface Effects and Couple Stress Theory Under Various Beam Theories

L. Shan
Zhengde Polytechnic College
M. Furjan
furjan@nua.edu.cn
Nanjing University of Aeronautics and Astronautics
I. M. Koç
Istanbul Technical University
E. Cigeroglu
Middle East Technical University
A. Cheraghbak
Islamic Azad University
M. H. Hajmohammad
Imam Hossein University
M. S. Zarei
Imam Hossein University

Research Article

Keywords: FG Microbeams, Metamaterials, CNT Composites, Surface Effects, Vibration and Acoustic Bandgap

Posted Date: March 25th, 2026

DOI: https://doi.org/10.21203/rs.3.rs-8877424/v1

License: This work is licensed under a Creative Commons Attribution 4.0 International License.
Read Full License

Additional Declarations: No competing interests reported.

Vibration and Acoustic Response of Metamaterial Micro-FG Beams Considering Surface Effects and Couple Stress Theory Under Various Beam Theories

L. Shan[a,b], M. Furjan[b,c]*, I.M. Koç[d,e], E. Cigeroglu[f,g], A. Cheraghbak[h], M.H. Hajmohammad[i], M.S. Zarei[i]

[a]Department of Automotive and Electromechanical Engineering, Zhengde Polytechnic College, Nanjing 211106, China
[b]International Joint Laboratory of Advanced Smart Structures and Control-NUAA, Nanjing 210016, China
[c]State Key Laboratory of Mechanics and Control for Aerospace Structures, Nanjing University of Aeronautics and Astronautics, Nanjing 210016, China
[d]International Joint Laboratory of Advanced Smart Structures and Control-ITU, Istanbul 34437, Turkey
[e]Department of Mechanical Engineering, Istanbul Technical University, İstanbul 34437, Turkey
[f]Department of Mechanical Engineering, Middle East Technical University, Ankara 06800, Turkey
[g]Center for Gear, Power Transmission and Vibration Research, Middle East Technical University, Ankara 06800, Turkey
[h]Department of Mechanical Engineering, Islamic Azad University, Jasb, Iran
[i]Department of Mechanical Engineering, Imam Hossein University, Tehran, Iran

*Corresponding author: furjan@nuaa.edu.cn (M.F.)

Abstract

In this paper, vibration and acoustic response of the metamaterial functionally graded (FG) microbeams are studied, which takes into account the surface effects based on the Gurtin-Murdoch theory of stress. The surface effects were explained using the Gurtin-Murdoch theory. The carbon nanotubes (CNTs) are used for the reinforcement of the microbeam, and the Mori-Tanaka model is applied to consider the impact of the nanoparticles and their agglomeration. The frequency and bandgap of the microstructure are obtained by using an analytical method. This paper will address and analyze the influence of the geometric parameters, the FG index, percentage of nanoparticles, and agglomeration, as well as the small-scale parameter, on the vibration of the microbeam. The FG metamaterial microbeam has a frequency that grows strongly with microbeam thickness and small-scale effects, with an increase in frequency up to 82% owing to the increased bending stiffness and 5.48T owing to size-dependent hardening. Effective stiffness varies with changes in frequency of reinforcement of nanoparticles by nanoparticles, frequency of reinforcement of agglomeration, and the gradient index of FGM, all of which reduce the frequency. The microbeam has a bandgap range of 1.0 x 10^7 Hz to 2.63 x 10^7 Hz, and it has been found to control the acoustic waves with local resonance.

Keywords: FG Microbeams; Metamaterials; CNT Composites; Surface Effects; Vibration and Acoustic Bandgap.

1-Introduction

Vibration and acoustic response analysis in micro-beams made of metamaterials is a critical problem since the effects of size-dependent behavior have a strong impact that cannot be considered through classical continuum mechanics. This intricate interaction is explored in this piece of work through the development of a complex model that considers the surface stresses, which are formulated using Gurtin-Murdoch theory, and micro-structural couple stresses in order to capture the mechanical behavior at the small scale. These phenomena are further studied by means of assessing them in the context of different beam theories, such as Euler-Bernoulli, Timoshenko, and higher-order shear deformable, to critically evaluate their predictive potentials on the dynamics of structure, as well as the resultant acoustic radiations. The overall goal is to clarify how the important parameters, which include the metamaterial structure, the intrinsic parameters of scale, and the selection of the kinematic assumptions, influence the nonlinear frequency response and the corresponding sound transmission characteristics, and hence serve as a guiding principle of the design of advanced devices of the micro-scale character with designed vibro-acoustic behavior.

The recent research and investigations show great interest in mechanical metamaterials because of their distinctive dynamics of impact and the possibility of absorbing the energy [1]. Sponge-inspired designs have shown initial innovations whereby dynamic mechanical behavior has been reported (tunable Poisson's ratios), thereby increasing their usefulness in construction and building materials [2]. Li et al. [3] advanced the design of metamaterial structures by incorporating configuration-dependent surface and nonlocal effects, enabling customized mechanical properties. Specifically, auxetic lattice metamaterials using partially-curved beam geometries have been optimized for energy absorption and stress response [4]. Also, aperiodic honeycomb metamaterials

with reinforcement have demonstrated good temperature-dependent compressive behavior, and it can be concluded that the material can be multifunctional [5]. Metamaterial Viscoelastic beam are now found to offer a convenient approach to integrate vibration isolation and energy harvesting, and this is a domain of adaptive material systems that has attracted increased attention [6]. The single-beam honeycomb metamaterials with tunable bandgap properties are useful in broadband vibration reduction and have shown potential to be used in vibration control technologies [7]. Wu et al. [8] have also investigated the effect of inherent geometrical nonlinearity on the attenuation of the flexural wave of a metamaterial beam, the result of which shows that dynamic performance is greatly influenced. The piezoelectric metamaterial beam optimization has been able to achieve active and tunable broadband vibration suppression, which has led to an increase in material functionality [9]. Guo et al. [10] have also demonstrated the multi-span metamaterial dual-beam structures with ultra-low-frequency vibration attenuation, which increases the range of metamaterial applications in vibration management. The Pancella and D'Annibale [11] have used Timoshenko-like equivalent beam methods as analytical models to study the mechanical behavior of chiral metamaterials, which have been very useful in their analysis. To enhance the work of metamaterials, novel multiple-beam designs with internal local resonance have been presented by Failla et al. [12]. Along with additional experimental and numerical research on the flexural vibration characteristics of carbon fiber-reinforced polymer metamaterial beams [13]. Another important step is the creation of a strong nonlinear elastic metamaterial that relies on collision damping [14]. Also, Furjan et al. [15] presented graded and disordered piezoelectric metamaterials that have been demonstrated to suppress broadband vibration, which has focused on versatility. Structural flexibility has been discussed and experimented with to be useful in energy harvesting, particularly in complicated non-sinusoidal pitching movements, which are part of optimizing semi-

active flapping foils [16]. The mechanical characteristics of new re-entrant auxetic structures with sinusoidal inclusions have been adjusted to obtain the desired in-plane characteristics by Chen et al. [17]. Xiao et al. [18] have studied how friction performance can be optimized by sinusoidal microtextures and the coupling of DLC coatings, and they have described their effects on reciprocating mechanisms of friction. Kumar and Verma [19] simulated and experimentally verified that solar air heaters with sinusoidal ribs are more thermally efficient. Vibration control has also been pushed to telescopic Timoshenko beams with questionable payloads, using adaptive control methods that are founded on the partial diffusion equation models [20]. Theoretical knowledge on beam mechanics has been enhanced by corrections in continuity conditions of beams whose equations are based on the Timoshenko-Ehrenfest equation [21]. The thermal effects of moving loads on transversely isotropic porous subgrades have been added to the performance analysis of the Timoshenko beam under moving loads [22]. The models of dynamic Timoshenko beam constraints have been developed on compliant mechanisms that experience intermediate ranges of deformation [23]. Timoshenko beams placed on a moving mass and based on fractional viscoelastic Pasternak foundations have also been studied, which has further complicated the analysis of vibrations [24]. Future research involves the investigation of vibration in piezoelectric Timoshenko beams under resistive-inductive electrodes. Schoeftner [25] presented the study of the beams with open cracks under moving masses. Brethee and Awad [26] studied the dynamic modeling of centrifugally stiffened proportionally damped Timoshenko beams. To learn about the mechanisms of energy dissipation [27], decay rates in Timoshenko beam systems in terms of nonlinear localized damping have been measured [28]. Nonlinear beams based on higher-order theory with nano shape memory alloy panel have been presented by Chu et al. [29]. Finally,

research on the forced vibration under harmonic excitation of a spherical cap has yielded some information about the nonlinear dynamics of beams by Furjan et al. [30].

The main originality of the work is the creation of a multi-scale model, which is unique because it combines a number of developed physical theories to describe the complicated vibro-acoustic behavior of micro-scale metamaterials. In contrast to past studies, the study concurrently uses the Gurtin-Murdoch surface stress theory, which is a couple stress model that takes into consideration micro-structural effects and the Mori-Tanaka homogenization scheme to a carbon nanoparticle-reinforced composite matrix, in a nonlinear dynamic context. Moreover, to provide a critical comparative analysis, the same unifying model is applied to a number of different beam theories (Euler-Bernoulli, Timoshenko, and others) to objectively measure the influence of various kinematic assumptions on the nonlinear vibrations and acoustic response predicted. Lastly, the work gives a parametric exploration of the geometric parameter synergies, the nanoparticle volume fraction, and the small-scale parameter with detailed analysis that is essential to the customization of next-generation metamaterial micro-beams in MEMS and acoustic engineered applications.

2-Formulation

Figure 1 depicts an FGM metamaterial microbeam that is reinforced with the CNTs and has with length L and a thickness h. In order to regulate the propagation of waves in such a structure, the vibration absorber system using two springs and two masses is taken into consideration, with the stiffness values of Kg_2 and Kg_3, and masses of M_2 and M_3. Moreover, based on the consideration of the aggregation effects of the reinforcement, the microbeam reinforced with CNTs is analyzed.

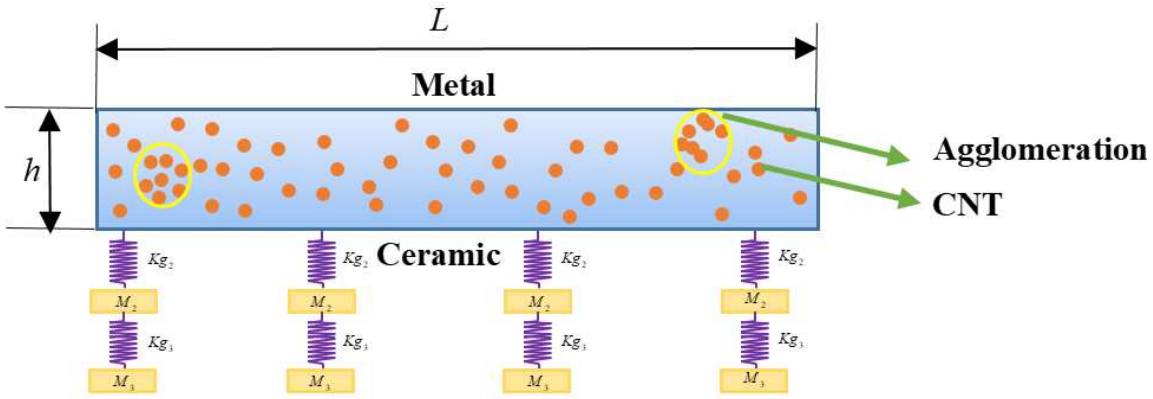


Fig. 1 An FGM metamaterial microbeam reinforced with the CNTs with vibration absorber system.

The field equations for displacement are as follows [31]:

$$U(x,z,t) = u(x,t) - z\frac{\partial}{\partial x}w(x,t) + f(z)\left(\frac{\partial}{\partial x}\gamma(x,t)\right), \tag{1}$$

$$W(x,z,t) = w(x,t). \tag{2}$$

In the above equations, u and w represent the displacements along the x and z axes, respectively.

Furthermore, the function $f(z)$ for different theories is defined as follows:

$f(z) = z$ Timoshenko theory

$f(z) = \dfrac{z\left(1-4z^2\right)}{3h^2}$ Reddy theory

$f(z) = \dfrac{h}{\pi}\sin\left(\dfrac{\pi z}{h}\right)$ Sinusoidal theory

$f(z) = ze^{-2(\frac{z}{h})^2}$ Exponential theory

The strain-displacement relationships are as follows:

$$\varepsilon_{xx} = \frac{\partial}{\partial x}U(x,z,t) = \frac{\partial}{\partial x}u(x,t) - z\left(\frac{\partial^2}{\partial x^2}w(x,t)\right) + f(z)\left(\frac{\partial^2}{\partial x^2}\gamma(x,t)\right), \tag{3}$$

$$\varepsilon_{xz} = \frac{1}{2}\left[\frac{\partial}{\partial z}U(x,z,t)+\frac{\partial}{\partial x}W(x,z,t)\right]=\frac{1}{2}\left(\frac{\partial}{\partial z}f(z)\right)\left(\frac{\partial}{\partial x}\gamma(x,t)\right). \tag{4}$$

Here, the Mori-Tanaka homogenization model is used to obtain the effective material properties of the reinforced metamaterial microbeam with CNTs. The micromechanical method takes into consideration the contact between the matrix and the dispersed CNTs and was a better measure of overall elastic and mechanical properties of the composite [32, 33]. Based on this model, we have below relation:

$$\begin{aligned}\sigma_{xx} &= (k+m)\varepsilon_{xx}\\ \sigma_{xz} &= (m)\varepsilon_{xz}\end{aligned} \tag{5}$$

where *k* and *m* are defined as below:

$$\begin{aligned}k &= \frac{E_m\{E_m c_m + 2k_r(1+\nu_m)[1+c_r(1-2\nu_m)]\}}{2(1+\nu_m)[E_m(1+c_r-2\nu_m)+2c_m k_r(1-\nu_m-2\nu_m^2)]}\\ m &= \frac{E_m[E_m c_m + 2m_r(1+\nu_m)(3+c_r-4\nu_m)]}{2(1+\nu_m)\{E_m[c_m+4c_r(1-\nu_m)]+2c_m m_r(3-\nu_m-4\nu_m^2)\}}\end{aligned} \tag{6}$$

in which E_m is the Young's modulus υ_m denotes the Poisson's ratio; C_m and C_r denote the matrix and the CNTs volume fractions respectively; k_r, m_r present the Hill's elastic modulus. If we assume the agglomeration of CNTs, the volume fraction of CNTs may be divided into two fractions of in ''inclusions'' ($V_r^{inclusion}$) and out of ''inclusions'' (V_r^{m}) as

$$V_r = V_r^{inclusion} + V_r^{m} \tag{7}$$

which ξ and ζ may be defined as:

$$\xi = \frac{V_{inclusion}}{V}, \tag{8}$$

$$\zeta = \frac{V_r^{inclusion}}{V_r}. \tag{9}$$

Also, the volume fraction of CNTs can be expressed as:

$$C_r = \frac{V_r}{V}. \tag{10}$$

The effective bulk modulus (K) and shear modulus (G) may be presented as:

$$K_{eff} = K_O \left[1 + \frac{\xi\left(\frac{K_I}{K_O} - 1\right)}{1 + \alpha\left(1-\xi\right)\left(\frac{K_I}{K_O} - 1\right)} \right] \quad , \tag{11}$$

$$G_{eff} = G_O \left[1 + \frac{\xi\left(\frac{G_I}{G_O} - 1\right)}{1 + \beta\left(1-\xi\right)\left(\frac{G_I}{G_O} - 1\right)} \right], \tag{12}$$

where

$$K_O = K_m + \frac{C_r\left(\delta_r - 3K_m\chi_r\right)\left(1-\zeta\right)}{3\left[1-\xi-C_r\left(1-\zeta\right)+C_r\chi_r\left(1-\zeta\right)\right]}, \tag{13}$$

$$K_I = K_m + \frac{\left(\delta_r - 3K_m\chi_r\right)C_r\zeta}{3\left(\xi - C_r\zeta + C_r\zeta\chi_r\right)}, \tag{14}$$

$$G_O = G_m + \frac{C_r\left(\eta_r - 3G_m\beta_r\right)\left(1-\zeta\right)}{2\left[1-\xi-C_r\left(1-\zeta\right)+C_r\beta_r\left(1-\zeta\right)\right]}, \tag{15}$$

$$G_I = G_m + \frac{\left(\eta_r - 3G_m\beta_r\right)C_r\zeta}{2\left(\xi - C_r\zeta + C_r\zeta\beta_r\right)}, \tag{16}$$

which $\chi_r, \beta_r, \delta_r, \eta_r$ may be expressed as:

$$\chi_r = \frac{3\left(K_m + G_m\right) + k_r - l_r}{3\left(k_r + G_m\right)}, \tag{17}$$

$$\beta_r = \frac{1}{5}\left\{\begin{array}{l}\dfrac{4G_m + 2k_r + l_r}{3\left(k_r + G_m\right)} + \dfrac{4G_m}{\left(p_r + G_m\right)} + \\ \dfrac{2\left[G_m\left(3K_m + G_m\right) + G_m\left(3K_m + 7G_m\right)\right]}{G_m\left(3K_m + G_m\right) + m_r\left(3K_m + 7G_m\right)}\end{array}\right\}, \tag{18}$$

$$\delta_r = \frac{1}{3}\left[n_r + 2l_r + \frac{\left(2k_r - l_r\right)\left(3K_m + 2G_m - l_r\right)}{k_r + G_m}\right], \tag{19}$$

$$\eta_r = \frac{1}{5}\left[\begin{array}{l}\dfrac{2}{3}\left(n_r - l_r\right) + \dfrac{4G_m p_r}{\left(p_r + G_m\right)} + \\ \dfrac{8G_m m_r\left(3K_m + 4G_m\right)}{3K_m\left(m_r + G_m\right) + G_m\left(7m_r + G_m\right)} + \\ \dfrac{2\left(k_r - l_r\right)\left(2G_m + l_r\right)}{3\left(k_r + G_m\right)}\end{array}\right]. \tag{20}$$

where

$$K_m = \frac{E_m}{3\left(1 - 2\upsilon_m\right)}, \tag{21}$$

$$G_m = \frac{E_m}{2\left(1 + \upsilon_m\right)}. \tag{22}$$

Also, β, α may be expressed as:

$$\alpha = \frac{\left(1 + \upsilon_{out}\right)}{3\left(1 - \upsilon_{out}\right)} \quad , \tag{23}$$

$$\beta = \frac{2\left(4 - 5\upsilon_{out}\right)}{15\left(1 - \upsilon_{out}\right)}, \tag{24}$$

$$\upsilon_{out} = \frac{3K_{out} - 2G_{out}}{6K_{out} + 2G_{out}}. \tag{25}$$

Lastly, the effective Poisson ratio (υ) and elastic modulus (E) of the nanocomposite microbeam may be given in terms of homogenized material characteristics of the Mori-Tanaka model. These

parameters describe the mechanical behavior of the composite reinforced by the nanoparticles in general and, as such, are the resultant product of the behavior of the matrix and the dispersed nanoparticles on the stiffness and deformation behavior of the composite. Hence, we have:

$$E = \frac{9KG}{3K + G}, \tag{26}$$

$$\upsilon = \frac{3K - 2G}{6K + 2G}. \tag{27}$$

By assuming the FG microbeam, the effective Poisson ratio and elastic modulus can be expressed as:

$$E(z) = E_{Metal} + \left(E_{Cerramic} - E_{Metal}\right)\left(\frac{1}{2} + \frac{z}{h}\right)^{m}, \tag{28}$$

$$\rho(z) = \rho_{Metal} + \left(\rho_{Cerramic} - \rho_{Metal}\right)\left(\frac{1}{2} + \frac{z}{h}\right)^{m}, \tag{29}$$

$$\upsilon(z) = \upsilon_{Metal} + \left(\upsilon_{Cerramic} - \upsilon_{Metal}\right)\left(\frac{1}{2} + \frac{z}{h}\right)^{m}, \tag{30}$$

where m is the FG index.

According to Hooke's law, the stress-strain equations are as follows:

$$\begin{aligned} \sigma_{xx} &= C_{11}\varepsilon_{xx} \\ \sigma_{xz} &= C_{55}\varepsilon_{xz} \end{aligned} \tag{31}$$

According to the above relations, the bulk and surface stresses are defined as follows.

$$\sigma_{xx} = C_{11}\left(\frac{\partial}{\partial x}u(x,t)\right) - C_{11}.z\left(\frac{\partial^2}{\partial x^2}w(x,t)\right) + C_{11}.f(z)\left(\frac{\partial^2}{\partial x^2}\gamma(x,t)\right) + C_{33}\sigma_{zz}, \tag{32}$$

$$\sigma_{xx}^{s} = C_{11}^{s}\left(\frac{\partial}{\partial x}u(x,t)\right) - C_{11}^{s}.z\left(\frac{\partial^2}{\partial x^2}w(x,t)\right) + C_{11}^{s}.f(z)\left(\frac{\partial^2}{\partial x^2}\gamma(x,t)\right), \tag{33}$$

$$\sigma_{xz} = C_{11}.f(z)^2\left(\frac{\partial}{\partial x}\gamma(x,t)\right), \tag{34}$$

$$\sigma_{xz}^{s} = \tau_s\left(\frac{\partial}{\partial x}W(x,z,t)\right), \tag{35}$$

$$\sigma_{zz} = \frac{(\frac{\partial\sigma_{xz}^{S}}{\partial x} - \rho_s\frac{\partial^2 w}{\partial t^2})\Big|_{\text{at top}} + (\frac{\partial\sigma_{xz}^{S}}{\partial x} - \rho_s\frac{\partial^2 w}{\partial t^2})\Big|_{\text{at bottom}}}{2} + \frac{(\frac{\partial\sigma_{xz}^{S}}{\partial x} - \rho_s\frac{\partial^2 w}{\partial t^2})\Big|_{\text{at top}} - (\frac{\partial\sigma_{xz}^{S}}{\partial x} - \rho_s\frac{\partial^2 w}{\partial t^2})\Big|_{\text{at bottom}}}{2h} z = \frac{\left[\tau_s\left(\frac{\partial^2}{\partial x^2}w(x,t)\right) - \rho_s\left(\frac{\partial^2}{\partial x^2}w(x,t)\right)\right]}{h} z \tag{36}$$

The strain gradient theory has been used to consider small-scale effects, which are as follows:

$$U_b = \frac{1}{2}\int_{\Omega}(\sigma_{ij}\varepsilon_{jk} + m_{ij}\chi_{ij})dV, \tag{37}$$

$$\varepsilon_{ij} = \frac{1}{2}\left(\frac{\partial u_j}{\partial x_i} + \frac{\partial u_i}{\partial x_j}\right), \tag{38}$$

$$\chi_{ij} = \frac{1}{2}\left(\frac{\partial\theta_i}{\partial x_j} + \frac{\partial\theta_j}{\partial x_i}\right),\ \theta_i = \frac{1}{2}e_{ijk}\frac{\partial u_k}{\partial x_j} = \frac{1}{2}\nabla\times\mathbf{u}, \tag{39}$$

$$\sigma_{ij} = k\,\delta_{ij}\varepsilon_{mm} + 2G\varepsilon_{ij}, \tag{40}$$

$$m_{ij} = 2l_0^2 G\,\chi_{ij}, \tag{41}$$

$$m_{xy} = 2.l^2.G.\chi_{xy} \tag{42}$$

$$m_{zy} = 2.l^2.G.\chi_{zy} \tag{43}$$

$$\chi_{xy} = \frac{1}{2}\left(\frac{\partial}{\partial x}\theta_j + \frac{\partial}{\partial x}\theta_i\right) = -\frac{1}{2}\frac{\partial^2}{\partial x^2}w(x,t) + \frac{1}{4}\left(\frac{\partial}{\partial z}f(z)\right)\left(\frac{\partial^2}{\partial x^2}\gamma(x,t)\right), \tag{44}$$

$$\chi_{zy} = \frac{1}{2}\left(\frac{\partial}{\partial y}\theta_k + \frac{\partial}{\partial z}\theta_j\right) = \frac{1}{4}\left(\frac{\partial^2}{\partial z^2}f(z)\right)\left(\frac{\partial}{\partial x}\gamma(x,t)\right), \tag{45}$$

The force components are defined as follows:

$$N_{xx} = \int_{-\frac{h}{2}}^{\frac{h}{2}} \sigma_{xx} dz + \sigma_{xx}^{s}\Big|_{\frac{h}{2}} + \sigma_{xx}^{s}\Big|_{-\frac{h}{2}} = A_{11}\frac{\partial}{\partial x}u(x,t) - B_{11}\frac{\partial^2}{\partial x^2}w(x,t) + E_{11}\frac{\partial^2}{\partial x^2}\gamma(x,t) + \\ + \frac{B_{33}\left(\tau_s\left(\frac{\partial^2}{\partial x^2}w(x,t)\right) - \rho_s\left(\frac{\partial^2}{\partial x^2}w(x,t)\right)\right)}{h}, \tag{46}$$

$$M_{xx} = \int_{-\frac{h}{2}}^{\frac{h}{2}} \sigma_{xx} z dz + \sigma_{xx}^{s} z\Big|_{\frac{h}{2}} + \sigma_{xx}^{s} z\Big|_{-\frac{h}{2}} = B_{11}\frac{\partial}{\partial x}u(x,t) - D_{11}\frac{\partial^2}{\partial x^2}w(x,t) + F_{11}\frac{\partial^2}{\partial x^2}\gamma(x,t) + \\ + \frac{D_{33}\left(\tau_s\left(\frac{\partial^2}{\partial x^2}w(x,t)\right) - \rho_s\left(\frac{\partial^2}{\partial x^2}w(x,t)\right)\right)}{h}, \tag{47}$$

$$M_{xc} = \int_{-\frac{h}{2}}^{\frac{h}{2}} \sigma_{xx} f(z) dz + \sigma_{xx}^{s} f(z)\Big|_{\frac{h}{2}} + \sigma_{xx}^{s} f(z)\Big|_{-\frac{h}{2}} = E_{11}\frac{\partial}{\partial x}u(x,t) - F_{11}\frac{\partial^2}{\partial x^2}w(x,t) + H_{11}\frac{\partial^2}{\partial x^2}\gamma(x,t) + \\ + \frac{F_{33}\left(\tau_s\left(\frac{\partial^2}{\partial x^2}w(x,t)\right) - \rho_s\left(\frac{\partial^2}{\partial x^2}w(x,t)\right)\right)}{h}, \tag{48}$$

$$Q_{xz} = \int_{-\frac{h}{2}}^{\frac{h}{2}} \sigma_{xz} dz + \sigma_{xz}^{s}\Big|_{\frac{h}{2}} + \sigma_{xz}^{s}\Big|_{-\frac{h}{2}} = B_{55}\frac{\partial^2}{\partial x^2}\gamma(x,t) + 2\tau_s\left(\frac{\partial}{\partial x}w(x,t)\right), \tag{49}$$

$$Y_1 = \int_{-\frac{h}{2}}^{\frac{h}{2}} m_{xy} dz + m_{xy}^{s}\Big|_{\frac{h}{2}} + m_{xy}^{s}\Big|_{-\frac{h}{2}} = -A_{55}.l^2\frac{\partial^2}{\partial x^2}w(x,t) + \frac{1}{2}.D_{55}.l^2\frac{\partial^2}{\partial x^2}\gamma(x,t), \tag{50}$$

$$Y_2 = \int_{-\frac{h}{2}}^{\frac{h}{2}} m_{xy} z^2 dz + m_{xy} z^2\Big|_{\frac{h}{2}} + m_{xy} z^2\Big|_{-\frac{h}{2}} = -D_{55}.l^2\frac{\partial^2}{\partial x^2}w(x,t) + \frac{1}{2}.B_{55}.l^2\frac{\partial^2}{\partial x^2}\gamma(x,t), \tag{51}$$

$$Y_3 = \int_{-\frac{h}{2}}^{\frac{h}{2}} m_{zy} dz + m_{zy}\Big|_{\frac{h}{2}} + m_{zy}\Big|_{-\frac{h}{2}} = \frac{1}{2}.E_{55}.l^2\frac{\partial}{\partial x}\gamma(x,t), \tag{52}$$

In the above relations, the elastic coefficients are defined as follows.

$$A_{11} = \int_{-\frac{h}{2}}^{\frac{h}{2}} c_{11} dz + c_{11}^s \Big|_{\frac{h}{2}} + c_{11}^s \Big|_{-\frac{h}{2}}, \tag{53}$$

$$B_{11} = \int_{-\frac{h}{2}}^{\frac{h}{2}} c_{11} z dz + c_{11}^s z \Big|_{\frac{h}{2}} + c_{11}^s z \Big|_{-\frac{h}{2}}, \tag{54}$$

$$D_{11} = \int_{-\frac{h}{2}}^{\frac{h}{2}} c_{11} z^2 dz + c_{11}^s z^2 \Big|_{\frac{h}{2}} + c_{11}^s z^2 \Big|_{-\frac{h}{2}}, \tag{55}$$

$$E_{11} = \int_{-\frac{h}{2}}^{\frac{h}{2}} c_{11}.f(z) dz + c_{11}^s.f(z) \Big|_{\frac{h}{2}} + c_{11}^s f(z) \Big|_{-\frac{h}{2}}, \tag{56}$$

$$H_{11} = \int_{-\frac{h}{2}}^{\frac{h}{2}} c_{11}.f(z)^2 dz + c_{11}^s.f(z)^2 \Big|_{\frac{h}{2}} + c_{11}^s f(z)^2 \Big|_{-\frac{h}{2}}, \tag{57}$$

$$F_{11} = \int_{-\frac{h}{2}}^{\frac{h}{2}} c_{11}.z.f(z) dz + c_{11}^s.z.f(z) \Big|_{\frac{h}{2}} + c_{11}^s.z.f(z) \Big|_{-\frac{h}{2}}, \tag{58}$$

$$B_{33} = \int_{-\frac{h}{2}}^{\frac{h}{2}} c_{33} z dz, \tag{59}$$

$$D_{33} = \int_{-\frac{h}{2}}^{\frac{h}{2}} c_{33} z^2 dz, \tag{60}$$

$$F_{33} = \int_{-\frac{h}{2}}^{\frac{h}{2}} c_{33} z.f(z) dz, \tag{61}$$

$$A_{55} = \int_{-\frac{h}{2}}^{\frac{h}{2}} c_{55} dz + c_{55}^s \Big|_{\frac{h}{2}} + c_{55}^s \Big|_{-\frac{h}{2}}, \tag{62}$$

$$D_{55} = \int_{-\frac{h}{2}}^{\frac{h}{2}} c_{55}\left(\frac{\partial}{\partial z} f(z)\right) dz + c_{55}^{s}.\left(\frac{\partial}{\partial z} f(z)\right)\Big|_{\frac{h}{2}} + c_{55}^{s}.\left(\frac{\partial}{\partial z} f(z)\right)\Big|_{-\frac{h}{2}}, \tag{63}$$

$$B_{55} = \int_{-\frac{h}{2}}^{\frac{h}{2}} c_{55}\left(\frac{\partial}{\partial z} f(z)\right)^{2} dz + c_{55}^{s}.\left(\frac{\partial}{\partial z} f(z)\right)^{2}\Big|_{\frac{h}{2}} + c_{55}^{s}.\left(\frac{\partial}{\partial z} f(z)\right)^{2}\Big|_{-\frac{h}{2}}, \tag{64}$$

$$E_{55} = \int_{-\frac{h}{2}}^{\frac{h}{2}} c_{55}.z.\left(\frac{\partial}{\partial z} f(z)\right)^{2} dz + c_{55}^{s}.z.\left(\frac{\partial}{\partial z} f(z)\right)^{2}\Big|_{\frac{h}{2}} + c_{55}^{s}.z.\left(\frac{\partial}{\partial z} f(z)\right)^{2}\Big|_{-\frac{h}{2}}, \tag{65}$$

Also, the structural moment of inertia coefficients are defined as follows:

$$I_0 = \int_{-\frac{h}{2}}^{\frac{h}{2}} \rho dz + \rho^{s}\Big|_{\frac{h}{2}} + \rho^{s}\Big|_{-\frac{h}{2}}, \tag{66}$$

$$I_1 = \int_{-\frac{h}{2}}^{\frac{h}{2}} \rho z dz + \rho^{s} z\Big|_{\frac{h}{2}} + \rho^{s} z\Big|_{-\frac{h}{2}}, \tag{67}$$

$$I_2 = \int_{-\frac{h}{2}}^{\frac{h}{2}} \rho z^{2} dz + \rho^{s} z^{2}\Big|_{\frac{h}{2}} + \rho^{s} z^{2}\Big|_{-\frac{h}{2}}, \tag{68}$$

$$I_3 = \int_{-\frac{h}{2}}^{\frac{h}{2}} \rho f(z) dz + \rho^{s} f(z)\Big|_{\frac{h}{2}} + \rho^{s} f(z)\Big|_{-\frac{h}{2}}, \tag{69}$$

$$I_4 = \int_{-\frac{h}{2}}^{\frac{h}{2}} \rho z f(z) dz + \rho^{s} z f(z)\Big|_{\frac{h}{2}} + \rho^{s} z f(z)\Big|_{-\frac{h}{2}}, \tag{70}$$

$$I_5 = \int_{-\frac{h}{2}}^{\frac{h}{2}} \rho f(z)^{2} dz + \rho^{s} f(z)^{2}\Big|_{\frac{h}{2}} + \rho^{s} f(z)^{2}\Big|_{-\frac{h}{2}}. \tag{71}$$

The potential energy of the structure is calculated as follows:

$$U_b = \frac{1}{2}\int_\Omega (\sigma_{ij}\varepsilon_{jk} + m_{ij}\chi_{ij})dV = \frac{1}{2}\int_\Omega (\sigma_{xx}\delta\varepsilon_{xx} + \sigma_{xz}\delta\varepsilon_{xz} + m_{xy}\delta\chi_{xy} + m_{zy}\delta\chi_{zy})dV =$$
$$\frac{1}{2}\int_\Omega \sigma_{xx}\left(\frac{\partial}{\partial x}\delta u(x,t) - z\left(\frac{\partial^2}{\partial x^2}\delta w(x,t)\right) + f(z)\left(\frac{\partial^2}{\partial x^2}\delta\gamma(x,t)\right)\right) +$$
$$\sigma_{xz}\left(\frac{1}{2}\left(\frac{\partial}{\partial z}f(z)\right)\left(\frac{\partial}{\partial x}\delta\gamma(x,t)\right)\right) + m_{xy}\left(-\frac{1}{2}\frac{\partial^2}{\partial x^2}\delta w(x,t) + \frac{1}{4}\left(\frac{\partial}{\partial z}f(z)\right)\left(\frac{\partial^2}{\partial x^2}\delta\gamma(x,t)\right)\right) +$$
$$m_{zy}\left(\frac{1}{4}\left(\frac{\partial^2}{\partial z^2}f(z)\right)\left(\frac{\partial}{\partial x}\delta\gamma(x,t)\right)\right)dV = \frac{1}{2}\int_\Omega \left(\begin{array}{l} -\frac{\partial N_{xx}}{\partial x}\delta u(x,t) - \left(\frac{\partial^2 M_{xx}}{\partial x^2}\delta w(x,t)\right) + \\ \left(\frac{\partial^2 M_{xc}}{\partial x^2}\delta\gamma(x,t)\right) + \frac{1}{2}\left(\frac{\partial}{\partial x}\delta u(x,t)\right)^2 \end{array}\right) - \quad (72)$$
$$\left(\frac{1}{2}\left(\frac{\partial}{\partial z}f(z)\right)\left(\frac{\partial Q_{xz}}{\partial x}\delta\gamma(x,t)\right)\right) + \left(-\frac{1}{2}\frac{\partial^2 Y_1}{\partial x^2}\delta w(x,t) + \left(\frac{\partial^2 Y_2}{\partial x^2}\delta\gamma(x,t)\right)\right) -$$
$$\left(\frac{1}{4}\left(\frac{\partial^2}{\partial z^2}f(z)\right)\left(\frac{\partial Y_3}{\partial x}\delta\gamma(x,t)\right)\right)dx$$

The kinetic energy of the structure is defined as follows:

$$\delta K = \int_0^l \int_A \rho\left(U(x,z,t)\delta\dot{U}(x,z,t) + W(x,z,t)\delta\dot{W}(x,z,t)\right)dAdz =$$
$$\left(-I_0\frac{\partial^2}{\partial t^2}u(x,t) + I_1\frac{\partial^3}{\partial x\partial t^2}w(x,t) - I_4\frac{\partial^2}{\partial t^2}\gamma(x,t)\right)\delta u(x,t)$$
$$-\int_\Omega -\left(I_0\frac{\partial^2}{\partial t^2}w(x,t) - I_1\frac{\partial^3}{\partial x\partial t^2}u(x,t) + I_2\frac{\partial^4}{\partial x^2\partial t^2}\gamma(x,t) - I_5\frac{\partial^3}{\partial x\partial t^2}\gamma(x,t)\right)\delta w(x,t) -$$
$$\left(I_3\frac{\partial^2}{\partial t^2}u(x,t) + I_4\frac{\partial^3}{\partial x\partial t^2}w(x,t) - I_5\frac{\partial^2}{\partial t^2}\gamma(x,t)\right)\delta\gamma(x,t)dx = 0 \quad (73)$$

To obtain the governing equations of the structure, Hamilton's principle has been used, and the governing equations are calculated as follows:

$$Eq_1 : \frac{\partial}{\partial x}N_{xx} - I_0\frac{\partial^2}{\partial t^2}u(x,t) + I_1\frac{\partial^3}{\partial x\partial t^2}w(x,t) - I_4\frac{\partial^2}{\partial t^2}\gamma(x,t), \quad (74)$$

$$Eq_2 : \frac{\partial^2}{\partial x^2}M_{xx} + \frac{\partial^2}{\partial x^2}Y_1 - I_0\frac{\partial^2}{\partial t^2}w(x,t) - I_1\frac{\partial^3}{\partial x\partial t^2}u(x,t) + I_2\frac{\partial^4}{\partial x^2\partial t^2}\gamma(x,t) - I_5\frac{\partial^3}{\partial x\partial t^2}\gamma(x,t), \quad (75)$$

$$Eq_3 : \frac{\partial}{\partial x} M_{xc} + \frac{1}{2}\frac{\partial}{\partial x} Y_2 - \frac{1}{2} Y_3 - Q_{xz} - I_3 \frac{\partial^2}{\partial t^2} u(x,t) + I_4 \frac{\partial^3}{\partial x \partial t^2} w(x,t) - I_5 \frac{\partial^2}{\partial t^2} \gamma(x,t), \tag{76}$$

$$Eq4 : M_2 \frac{\partial^2}{\partial t^2} u_2(x,t) + k_2 \left[u_2(x,t) - w_2(x,t)\right] + k_3 \left[u_2(x,t) - u_3(x,t)\right], \tag{77}$$

$$Eq5 : M_3 \frac{\partial^2}{\partial t^2} u_3(x,t) + k_3 \left[u_3(x,t) - u_2(x,t)\right]. \tag{78}$$

An infinite periodic structure that has dynamic properties can be conveniently resolved by examining one representative unit cell and using the concepts of the Bloch-Floquet theory [26]. The effect of this is that the problem is greatly simplified because it takes advantage of the structure's periodicity, whereby the behavior of the global waves is commonly inferred based on the response of the repeated structure. Based on this, the elastic wave pulse, which travels along the unit cell, as shown in Fig. 1, can be taken to have a periodic form that obeys the Bloch-Floquet boundary conditions, and is therefore continuous and has phase consistency between the neighboring cells:

$$u(x,t) = P_u e^{(-i\Omega t + \beta x)} \tag{79}$$

$$w(x,t) = P_w e^{(-i\Omega t + \beta x)} \tag{80}$$

$$\gamma(x,t) = P_\gamma e^{(-i\Omega t + \beta x)} \tag{81}$$

$$u_2(x,t) = P_{u2} e^{(-i\Omega t + \beta x)} \tag{82}$$

$$u_3(x,t) = P_{u3} e^{(-i\Omega t + \beta x)} \tag{83}$$

where β denotes the wavenumber; Ω denotes the vibration frequency. With the help of Eqs. (79)-(83) into Eqs. (74)-(78) yields:

$$\left[\underbrace{\begin{bmatrix} k_{11} & k_{12} & k_{13} & k_{14} & k_{15} \\ k_{21} & k_{22} & k_{23} & k_{24} & k_{25} \\ k_{31} & k_{32} & k_{33} & k_{34} & k_{35} \\ k_{41} & k_{42} & k_{43} & k_{44} & k_{45} \\ k_{51} & k_{52} & k_{53} & k_{54} & k_{55} \end{bmatrix}}_{K} - \Omega^2 \underbrace{\begin{bmatrix} m_{11} & m_{12} & m_{13} & m_{14} & m_{15} \\ m_{21} & m_{22} & m_{23} & m_{24} & m_{25} \\ m_{31} & m_{32} & m_{33} & m_{34} & m_{35} \\ m_{41} & m_{42} & m_{43} & m_{44} & m_{45} \\ m_{51} & m_{52} & m_{53} & m_{54} & m_{55} \end{bmatrix}}_{M}\right] \begin{bmatrix} P_u \\ P_w \\ P_\gamma \\ P_{u2} \\ P_{u3} \end{bmatrix} = \begin{bmatrix} 0 \\ 0 \\ 0 \\ 0 \\ 0 \end{bmatrix} \tag{84}$$

where k_{ij} and m_{ij} are presented in Appendix A.

3-Results

To investigate the results of this article, a micro FGM beam is assumed with a length to thickness ratio of 5, metal properties $\left(E_m = 70Gpa,\ \rho_m = 2702Kg/m^3,\ \upsilon_m = 0.3\right)$, ceramic properties $\left(E_c = 427Gpa,\ \rho_c = 3100Kg/m^3,\ \upsilon_c = 017.3\right)$, and a small-scale coefficient $17\mu m$. This micro FGM beam is reinforced with CNTs with an elastic modulus of 1 TPa and a Poisson's ratio of 0.3 [32]. In its attempt to determine the validity of the current model, this section initiates a comparative validation of the already known work of Simsek and Reddy [34] as shown in Table 1. To facilitate this direct comparison and to keep the basis of the current analysis consistent, we have intentionally neglected the contribution of surface effects and nanoparticle interactions to the current analysis. This strategy enables the unambiguous and unambiguous validation of the core formulation that was applied in this study and the defined benchmark.

Table 1 Dimensionless fundamental frequency of the FC microbeam [34].

h/l	Theory	L/h = 10				L/h = 100			
		k = 0.3	k = 1	k = 3	k = 10	k = 0.3	k = 1	k = 3	k = 10
1	EBBT [32]	12.9004	10.6483	8.9420	7.8011	12.9565	10.6987	8.9845	7.8348
	FSDBT [32]	12.6058	10.3982	8.7110	7.5835	12.9533	10.6960	8.9820	7.8325
	PSDBT [32]	12.8337	10.6009	8.9048	7.7640	12.9558	10.6982	8.9841	7.8345
	TSDBT [32]	12.8344	10.6004	8.9034	7.7620	12.9558	10.6982	8.9841	7.8344
	HSDBT [32]	12.8337	10.6010	8.9050	7.7642	12.9558	10.6982	8.9841	7.8345
	ESDBT [32]	12.8364	10.6009	8.9027	7.7611	12.9558	10.6982	8.9840	7.8344
	Present	12.6522	10.4387	8.7486	7.6203	12.9525	10.6966	8.9828	7.8349
2	EBBT [32]	7.9307	6.6159	5.7362	5.1231	7.9651	6.6471	5.7633	5.1453
	FSDBT [32]	7.8233	6.5211	5.6383	5.0237	7.9640	6.6461	5.7623	5.1442
	PSDBT [32]	7.8722	6.5670	5.6876	5.0731	7.9645	6.6466	5.7628	5.1448

	TSDBT [32]	7.8725	6.5666	5.6861	5.0713	7.9645	6.6466	5.7628	5.1447
	HSDBT [32]	7.8722	6.5671	5.6878	5.0733	7.9645	6.6466	5.7628	5.1448
	ESDBT [32]	7.8735	6.5668	5.6853	5.0705	7.9645	6.6466	5.7628	5.1447
	Present	7.8395	6.5367	5.6546	5.0413	7.9628	6.6465	5.7629	5.1459
4	EBBT [32]	6.0840	5.1348	4.5978	4.1945	6.1104	5.1590	4.6195	4.2126
	FSDBT [32]	6.0115	5.0692	4.5256	4.1184	6.1096	5.1583	4.6187	4.2118
	PSDBT [32]	6.0236	5.0783	4.5327	4.1276	6.1097	5.1584	4.6188	4.2119
	TSDBT [32]	6.0237	5.0780	4.5316	4.1267	6.1097	5.1584	4.6188	4.2119
	HSDBT [32]	6.0236	5.0784	4.5328	4.1277	6.1097	5.1584	4.6188	4.2119
	ESDBT [32]	6.0242	5.0781	4.5310	4.1264	6.1097	5.1584	4.6188	4.2119
	Present	6.0218	5.0801	4.5387	4.1320	6.1081	5.1586	4.6192	4.2133
8	EBBT [32]	5.5267	4.6920	4.2659	3.9282	5.5507	4.7141	4.2861	3.9452
	FSDBT [32]	5.4617	4.6327	4.1995	3.8573	5.5500	4.7135	4.2854	3.9444
	PSDBT [32]	5.4646	4.6313	4.1922	3.8528	5.5500	4.7134	4.2853	3.9444
	TSDBT [32]	5.4645	4.6311	4.1915	3.8526	5.5500	4.7134	4.2853	3.9444
	HSDBT [32]	5.4645	4.6314	4.1923	3.8528	5.5500	4.7134	4.2853	3.9444
	ESDBT [32]	5.4649	4.6312	4.1912	3.8528	5.5500	4.7134	4.2853	3.9444
	Present	5.4707	4.6426	4.2107	3.8701	5.5484	4.7138	4.2864	3.9446
Classical theory	EBBT [32]	5.3280	4.5348	4.1494	3.8353	5.3511	4.5561	4.1691	3.8519
	FSDBT [32]	5.2654	4.4775	4.0848	3.7661	5.3505	4.5555	4.1684	3.8512
	PSDBT [32]	5.2649	4.4723	4.0719	3.7564	5.3504	4.5555	4.1682	3.8511
	TSDBT [32]	5.2650	4.4722	4.0715	3.7565	5.3504	4.5555	4.1682	3.8511
	HSDBT [32]	5.2649	4.4724	4.0720	3.7564	5.3504	4.5555	4.1682	3.8511
	ESDBT [32]	5.2652	4.4722	4.0713	3.7568	5.3504	4.5555	4.1682	3.8511
	Present	5.7765	4.4834	4.1213	3.7875	5.3654	4.5632	4.1697	3.8547

Figure 2 shows the impact of the parameter of the volume fraction on the dimensionless frequency of varying thicknesses. As it can be deduced, the frequency rises with the rise in the volume fraction as indicated in the graph. Besides, the frequency also rises 82% as the thickness of the structure rises from 15 μm to 30 μm. This is because the thickness is increased, which increases the stiffness of the structure, and as stiffness is directly proportional to the frequency, the frequency of the structure consequently increases. Figure 3 studies the influence of the percentage of volume of nanoparticles on the dimensionless frequency of varying values of the small-scale parameter. As may be noticed on the graph, the dimensionless frequency of the structure also grows 5.48% with the increase of the small-scale parameter coefficient from 15 μm to 30 μm. This effect can be explained by the fact that the further increase of the small-scale parameter makes the structure stiffer, thus causing the increase of the dimensionless frequency.

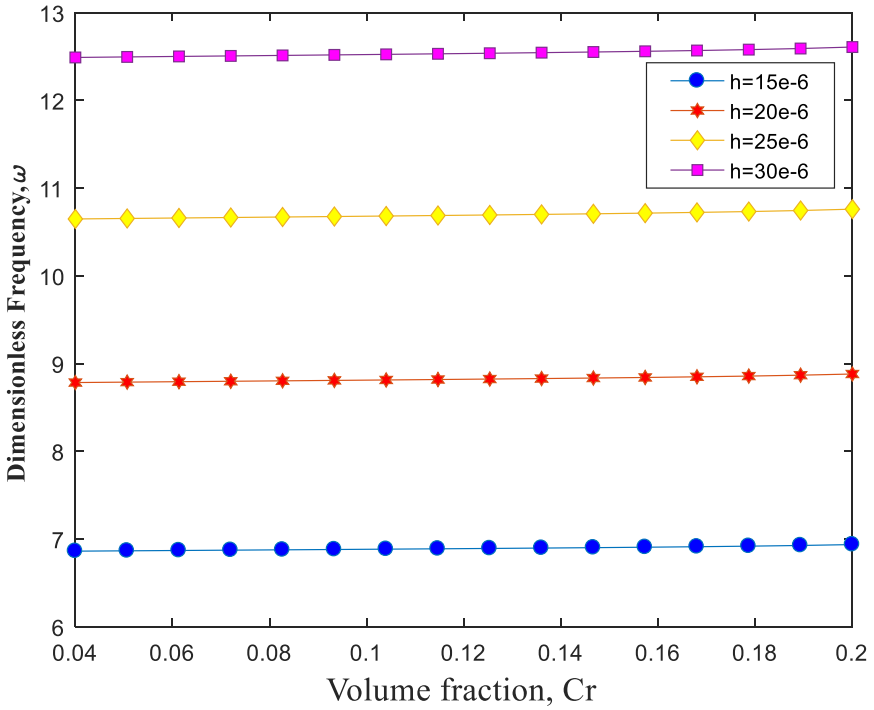


Fig. 2 The impact of the parameter of volume fraction of nanoparticles on the dimensionless frequency for various thicknesses.

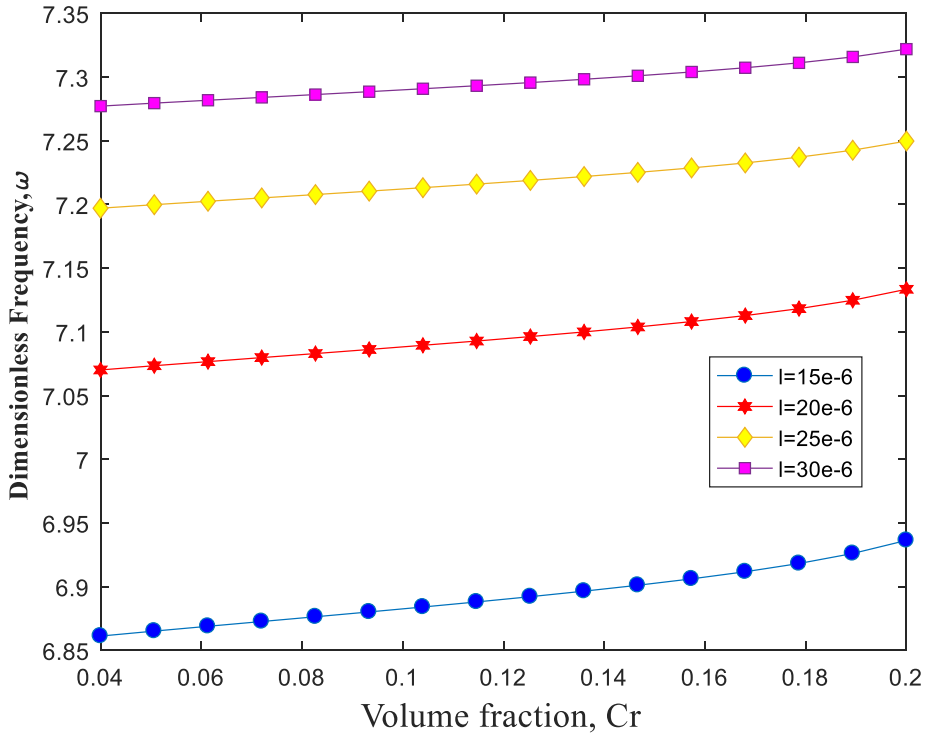


Fig. 3 The effect of the volume fraction of nanoparticles on the dimensionless frequency with different small-scale coefficients.

Figure 4 depicts how the percentage of the volume of nanoparticles affects the dimensionless frequency of the various theories. The gap between the theory of Timoshenko and the other theories is quite notable, as it should be deduced from the diagram. This is because the theory proposed by Timoshenko is not as accurate as the other theories. Also, the disparities of the other theories are not significant.

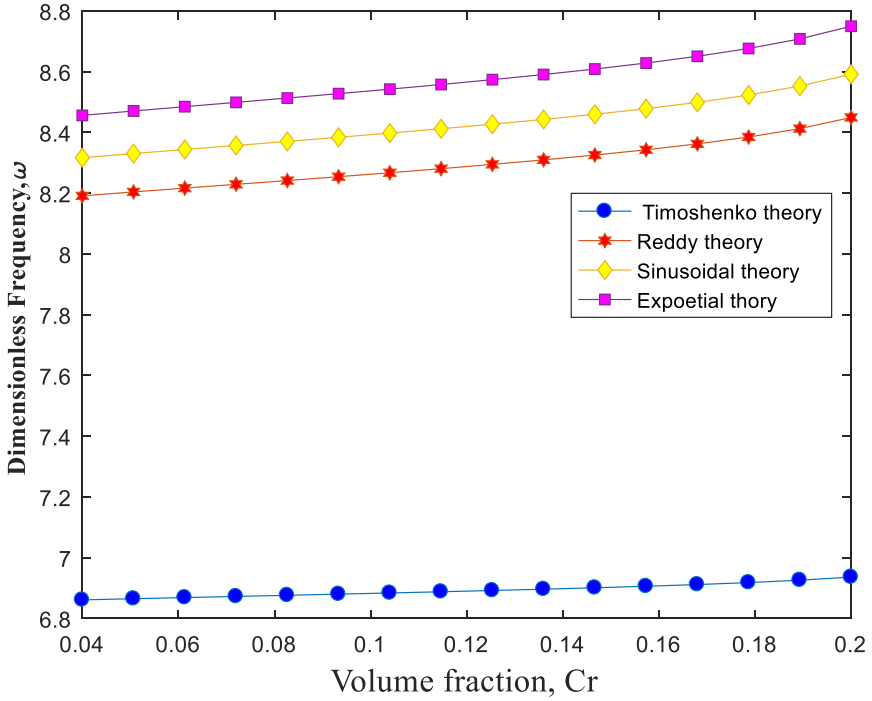


Fig. 4 The dimensionless frequency versus volume fraction of the nanoparticle according to various theories.

By plotting the thickness of the microbeam versus the dimensionless frequency in Figure 5, it is obvious that there are two behaviors. The mechanism of the physical origin of the growth of the dimensionless frequency as the thickness increases is the increase in the bending stiffness. The stiffness increases that cause the beam to become stiffer, giving it larger natural vibration frequencies. The second effect is the size effect. Considering the size effect, size-sensitive effects of changing the elasticity modulus or the appearance of residual stresses during fabrication appear.

These supplementary effects are usually linked to a decrease in the effective structural stiffness or an increment in components that diminish the structural stiffness, which eventually causes a decrease in the overall stiffness of the beam and, thus, a decrease in the natural vibration frequency than that of the situation without the size effect.

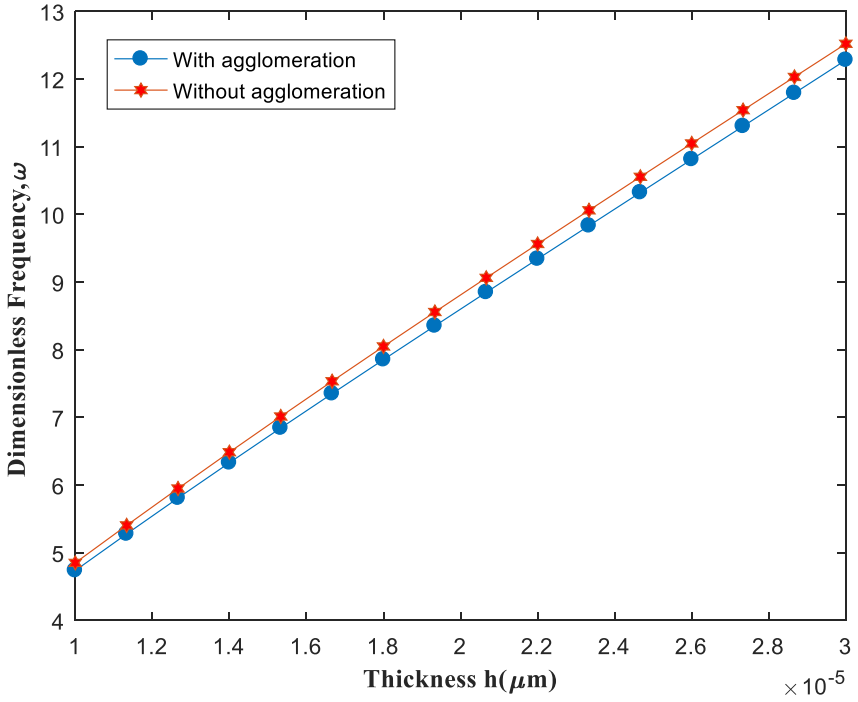


Fig. 5 The thickness of microbeams influences the dimensionless frequency in both cases with and without size effect.

Figure 6 shows how the dimensionless frequency varies as the thickness parameter is varied at the various values of the small-scale coefficient. As it is seen in the graph, the small-scale coefficient is positively correlated with the dimensionless frequency. This physical explanation of this behavior lies in the non-classical continuum mechanics theories, including the strain gradient elasticity theory. In these theories, the small-scale coefficient takes into consideration an additional stiffening effect that arises at the micron and sub-micron scales, in consideration of the long-range atomic interactions, as well as resistance against strain gradients. Therefore, a big small-scale coefficient is indicative of a greater size-dependent stiffening effect, which will increase the total

effective stiffening of the microbeam. Because the square root of the ratio of the stiffness to the mass is directly proportional to the natural vibration frequency, this increase in effective stiffness will eventually result in an increased dimensionless frequency.

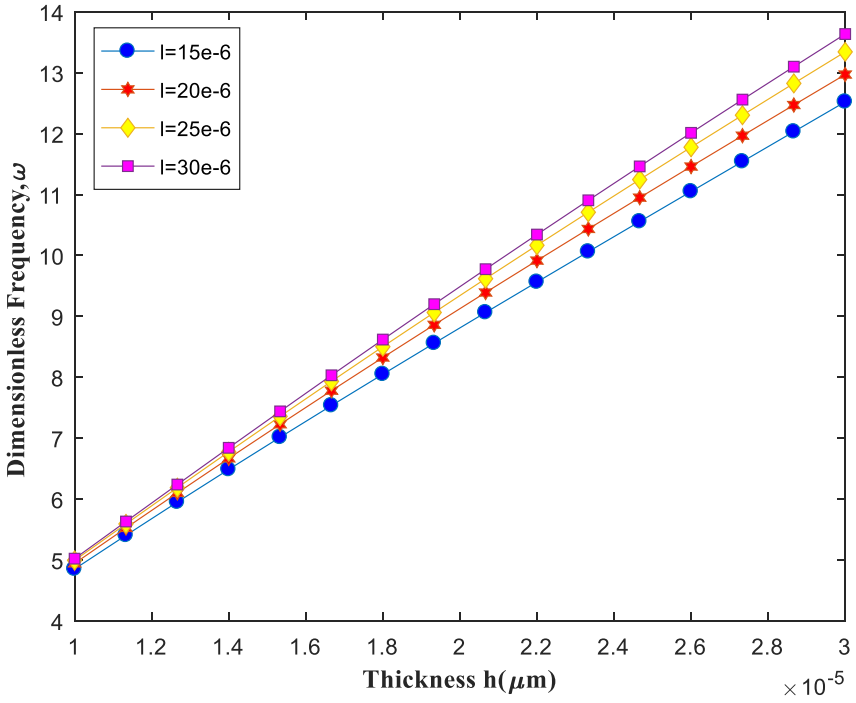


Fig. 6 The impact of the microbeam thickness on the dimensionless frequency at varying values of the small-scale coefficient.

The impact of microbeam thickness on the non-dimensional frequency of various theories is presented in Figure 7. Respectively, as observed in the figure, the deviation of the theory of Timoshenko and the other theories is very high, and this means that the theory of Timoshenko is not as accurate as the other theories. In other words, the results of Timoshenko theory are about 7.75% lower with respect to higher order theory of exponential.

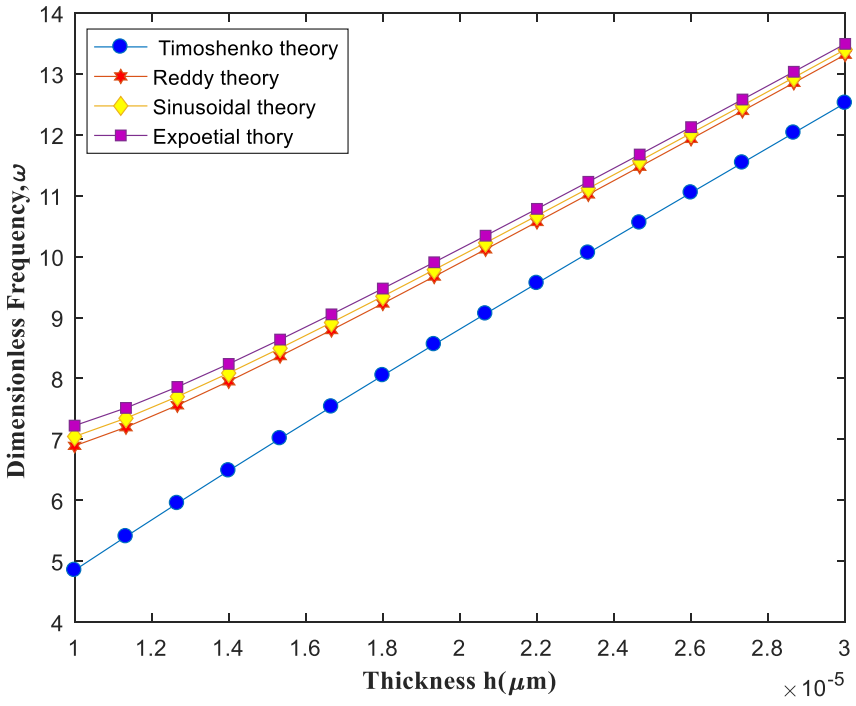


Fig. 7 The impact of the thickness parameter on the non-dimensional frequency for different theories.

Figure 8 indicates how the small-scale parameter varies the non-dimensional frequency with the various values of microbeam thickness. The frequency, as can be observed in the graph, is proportional to the small-scale coefficient. Moreover, the non-dimensional frequency is also increasing with the increase in the thickness of the microbeam. This is caused by the fact that when both parameters increase, the structural stiffness increases, and the relationship is direct between the stiffness and the frequency.

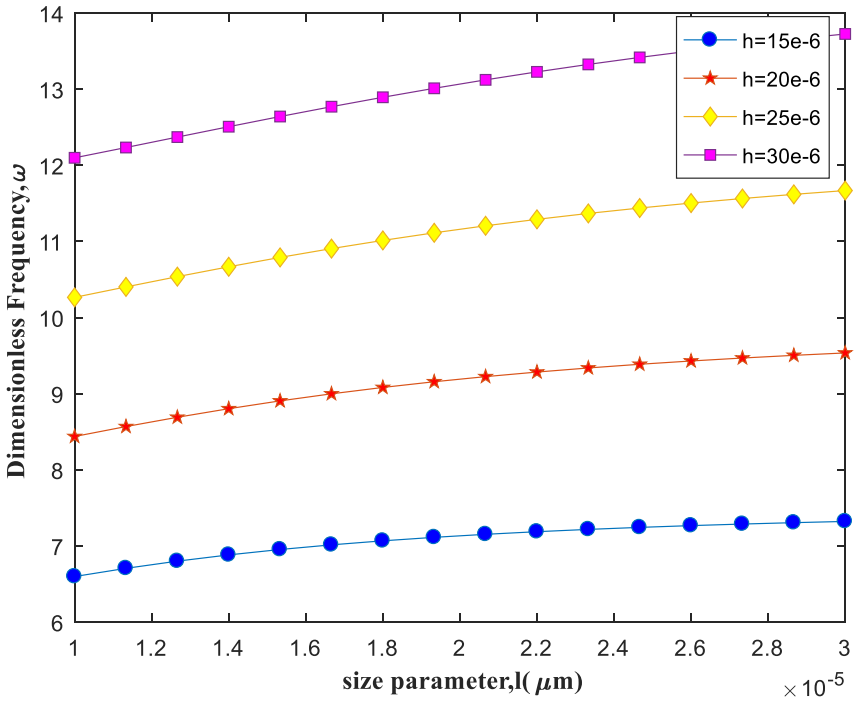


Fig. 8 The influence of the small-scale parameter on different thicknesses frequency.

As seen in Figure 9, the non-dimensional frequency of different nanoparticle volume fractions is affected by the small-scale parameter. The non-dimensional frequency increases as the volume proportion of nanoparticles rises, as the graph illustrates. This has been attributed to an intrinsic increase in the microbeam's structural rigidity. The physical justification for this is that the material's overall mechanical properties are improved when tougher and stiffer nanoparticles are added to the basic matrix. The compound structure will be more robust and solid the higher the volume % of these nanoparticles. This higher rigidity raises the natural frequency of the system directly, since it is the stiffer a structure the higher the frequency it will tend to resist deformation, and the higher the frequency, as a system. Moreover, this larger stiffness interacts with the small-scale parameter that provides the size-dependent effects that are domineering in the micro-scale but result in the trend observed in non-dimensional frequency among the various volume fractions.

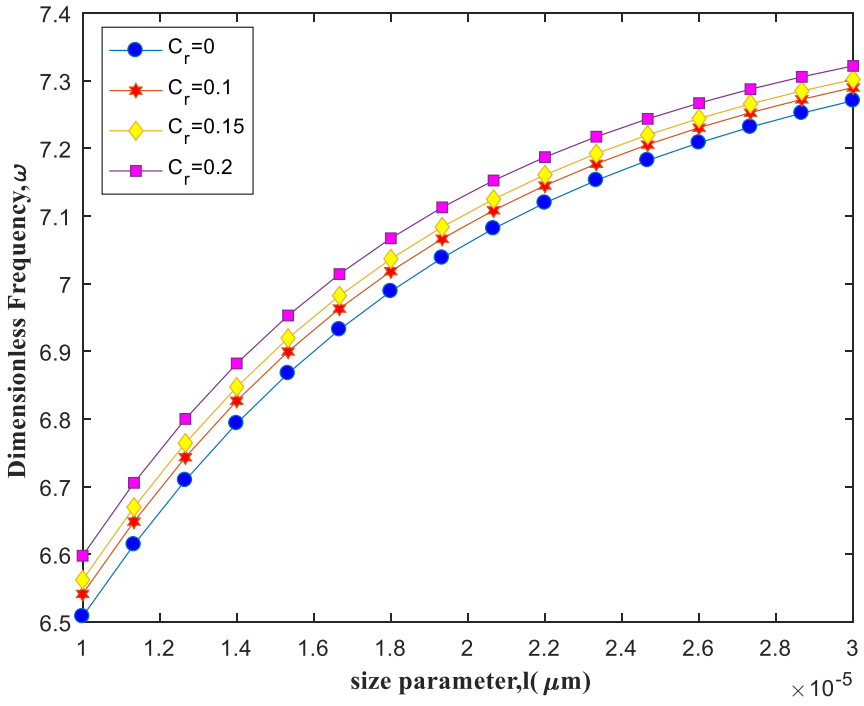


Fig. 9 Non-dimensional frequency of various volume percentages as a function of the small-scale parameter.

The impact of the small-scale parameter on the non-dimensional frequency was shown in Figure 10, comparing the ones with agglomeration effect and the ones without it. As can be seen in the graph, once the agglomeration of nanoparticles is taken into account, the non-dimensional frequency goes down. The fundamental physical change in the composite material brought about by agglomeration explains this drop. First, agglomeration disrupts the uniform distribution of the nanoparticles in the matrix by causing them to cluster. The overall dynamic properties of the structure are altered by this non-uniformity, which creates localized regions with significantly higher mass and stiffness. By increasing the localized mass in this process and ultimately decreasing the system's natural frequencies, these clusters increase the system's inertia. Agglomeration can also make it more difficult for the nanoparticles and matrix to transfer stress effectively, which could reduce the overall structural stiffness and lower the frequency. This is due

to the fact that, like in the simplistic models, the vibrational frequency would be exaggerated if the agglomeration effect were ignored. The agglomeration effect is a tangible phenomenon that must be taken into account in practical microstructural modeling.

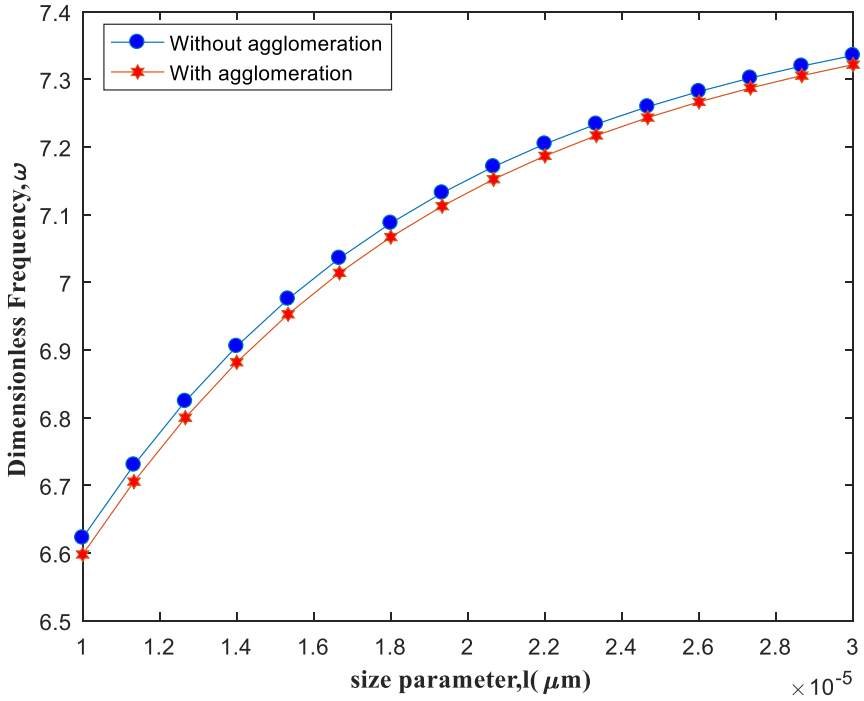


Fig. 10 The small-scale parameter influences on the non-dimensional frequency, considering the cases either with or without the agglomeration effect.

Figure 13 displays a bar chart that illustrates how the non-dimensional frequency at different thicknesses is affected by the volume percentage of nanoparticles. According to the graph, the frequency increases as thickness increases. This loss in precision can be explained by the fact that the theory of Timoshenko has certain limitations when it comes to the modeling of small-scale processes. Although the Timoshenko theory is an effective way of modelling shear effects and rotational inertia, it cannot fully explain the non-local effects and strain gradient stresses as those found in more complex theories like the strain gradient theory. As the significance of the small-scale parameter increases, it becomes increasingly evident that the Timoshenko theory's predictions do not align with the findings of other, more comprehensive theories. In particular, the

higher-order theories give a more realistic prediction of the structural frequency response, which is the added stiffness contribution, at micro and nano scales, under the influence of strain gradients and size-dependent effects. The attribute makes the Timoshenko theory approximate the non-dimensional frequency values with larger error than the more sophisticated theories, particularly when the small-scale effects in the system are eminent.

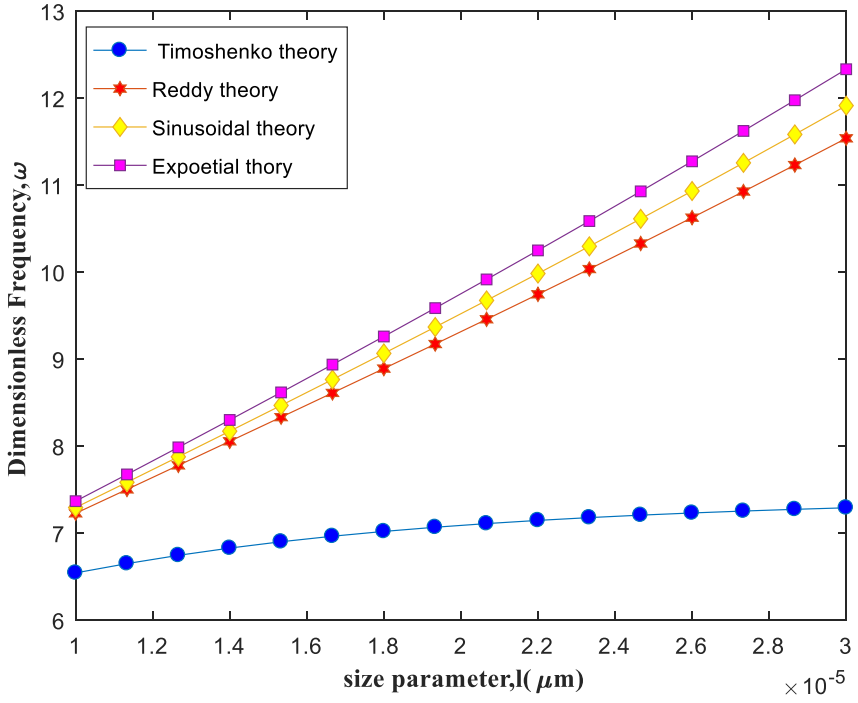


Fig. 11 The impact of the small-scale parameter on non-dimensional frequency for various theories.

Figure 12 shows a bar chart that shows how the non-dimensional frequency varies with the percentage of volume of nanoparticles in two cases, considering and not considering the agglomeration effect. As seen in the chart, the percentage of nanoparticle volume increases the non-dimensional frequency of both systems, which is mainly caused by the fact that the stiffness and the elastic modulus of the composite are increased by the introduction of hard nanoscale particles. But the most important fact is that, on taking agglomeration effects into consideration,

the rate of such increase is found to be significantly lower than that in the ideal situation, the non-agglomeration case. The mechanical cause of such behavior lies in the creation of a nanoparticle agglomerate, which causes its non-uniform distribution and dispersion in the base matrix. This phenomenon does not allow the nanoparticles to strongly and completely strengthen the matrix since agglomerates serve as a source of stress concentration and may even result in local undermining of the structure. They therefore do not contribute as much to the overall stiffness of the composite as they do in a case where there is a uniform distribution. Thus, the natural frequency of the system is directly proportional to the square root of the product of the stiffness and mass ratio increases at a slower rate. This analogy strongly reminds us of the need to have the agglomeration phenomenon fitted into proper modeling and prediction of the dynamic behavior of nanoparticle-reinforced composites.

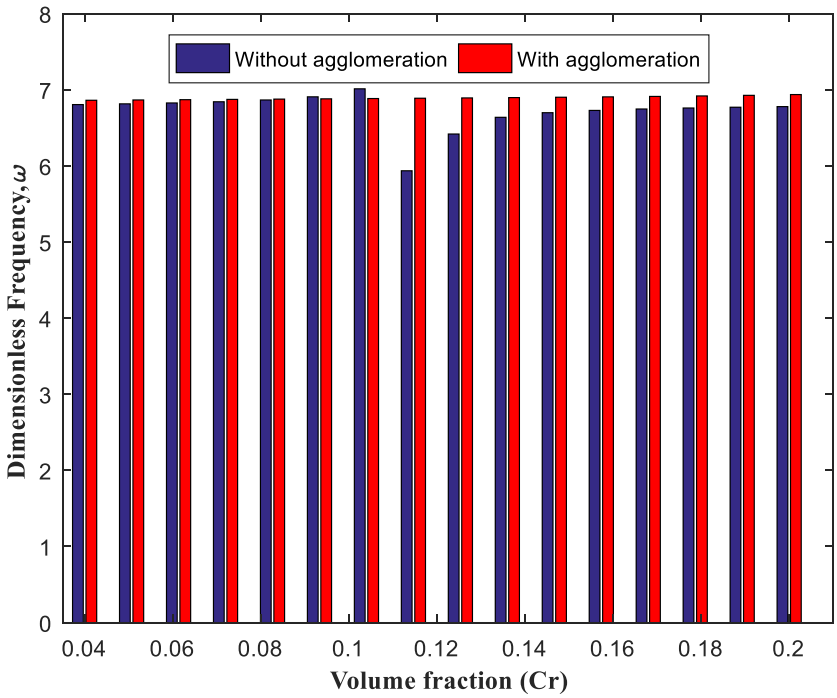


Fig. 12 The bar chart for the effect of nanoparticle volume percentage on the non-dimensional frequency with and without agglomeration effects.

A bar chart illustrating the effect of the volume percentage of nanoparticles on the non-dimensional frequency at different thicknesses is presented in Figure 13. The graph indicates that the frequency increases as thickness increases. This trend is essentially dictated by the thickness and the bending stiffness of the structure. Bending stiffness (D) depends on the thickness (h) as $h^{3,}$ and thus, the slightest addition to the thickness leads to a significant change in the structure's resistance to deformation. The fact that the natural frequency of a vibrating structure is proportional to the square root of the ratio of stiffness/mass means that the drastic increase in bending stiffness is overwhelming the subsequent, not as dramatic, increase in mass. This increases the overall ratio of stiffness to mass, giving rise to a higher natural frequency. The effect of nanoparticles further adds to the effective elastic modulus of the composite material, which adds to the stiffness and hence synergistically increases the frequency, and here it is higher in thicker structures because they are already stiff.

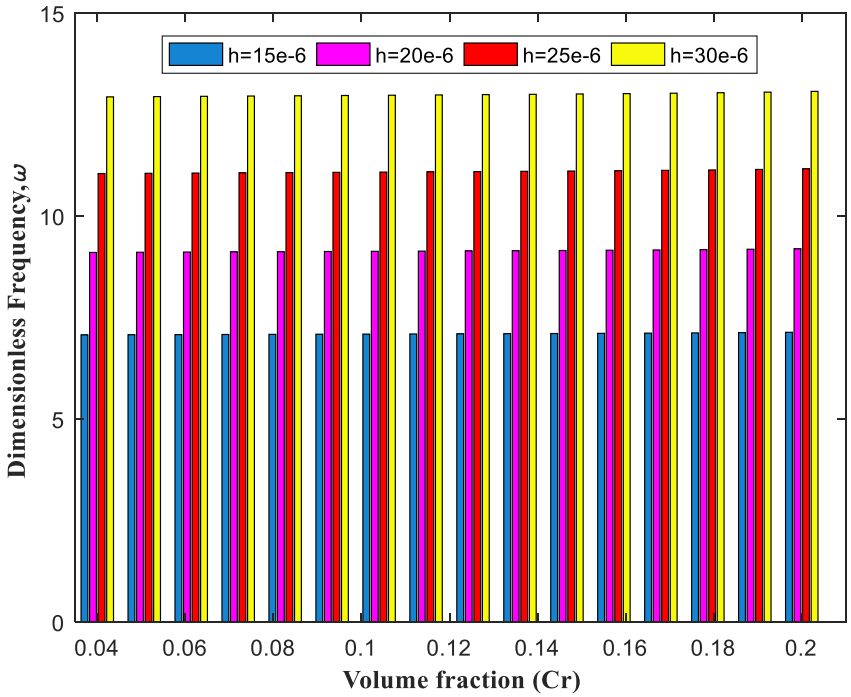


Fig. 13 The bar chart of the effect of nanoparticle volume percentage on the non-dimensional frequency for different thicknesses.

Figure 14 shows a bar chart that shows how the volume percentage of nanoparticles affects the non-dimensional frequency with various values of the small-scale parameter. According to what the chart suggests, there is a growth of non-dimensional frequency with the growth of the small-scale parameter. This noted tendency could be traced back to the basic physical mechanism embodied in the non-local and strain gradient elasticity models, in which the small-scale parameter brings in extra stiffness terms to the constitutive behavior of the material. Since this parameter increases, it improves the deformation resistance of the material at the micro-scale by considering long-range atomic interactions and strain gradient effects, which are not considered in classical continuum mechanics. This really augments the total structural stiffness (K) with no proportional increment in mass (M).

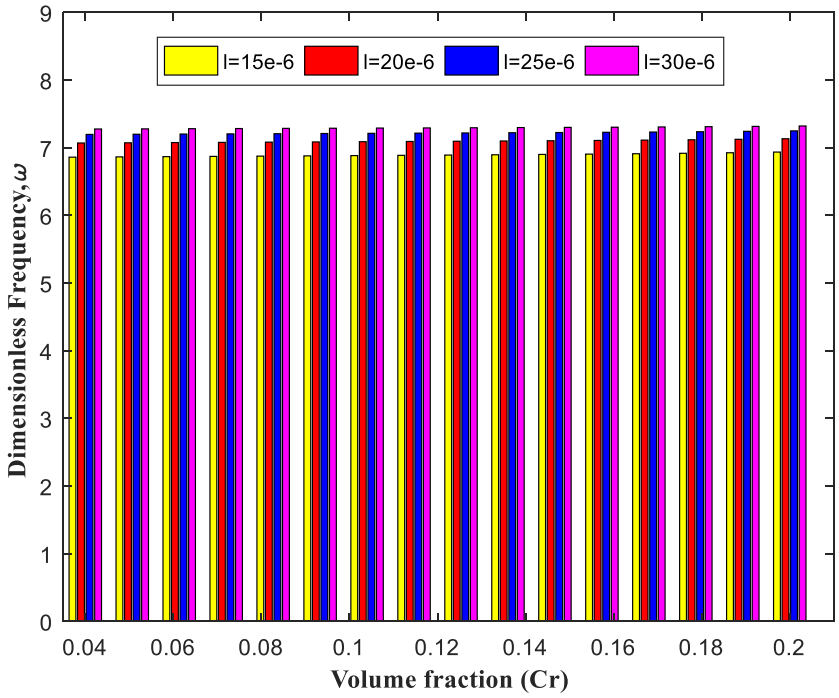


Fig. 14 The bar chart for the effect of the percentage of nanoparticle volume on the non-dimensional frequency in the various small-scale parameter values.

The fact that the natural frequency varies simply as the square root of the product of stiffness and mass of the object that vibrates, the augmented stiffness directly results in the observed increase

of non-dimensional frequency values at all nanoparticle volume percentages, and, therefore, on the very small scales, the effect of stiffness is very strong.

Figure 15 shows the bar chart of the percentage of nanoparticle volume on non-dimensional frequency at various values of FGM property gradient index. As can be concluded in the chart, the non-dimensional frequency decreases with the increase in the index of FGM gradient. This negative association is a literal effect of the impact of the gradient index on the distribution of material properties by the thickness of the structure. An increased gradient index indicates a more drastic change in material composition, which normally results in an increasing volume fraction of the less stiff constituent material (e.g., the metallic phase) in the regions of the structure cross-section in which the shear stresses are greatest (the outer fibers).

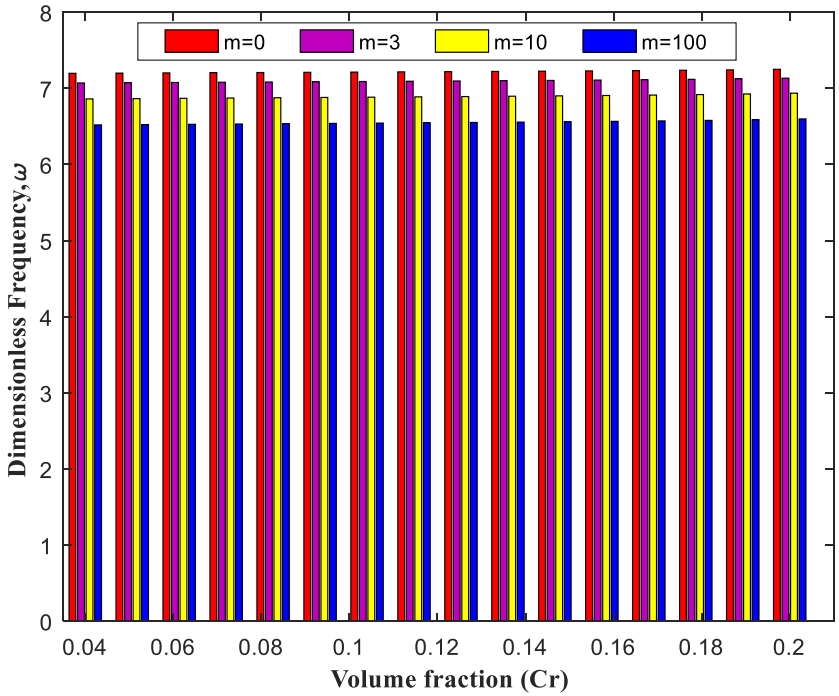


Fig. 15 The bar chart of nanoparticle volume percentage's effect on the non-dimensional frequency for different values of the functionally graded material coefficient.

This re-distribution is useful in softening the total flexural rigidity (or bending stiffness) of the structure. Because the natural frequency is inversely proportional to the square root of the product

of stiffness to mass, this decrease in the effective stiffness (K) prevails over any small alterations in the mass distribution, leading to an overall decrease in the non-dimensional frequency calculated.

The bar graph in Figure 16 shows the relationship between the non-dimensional frequency and the volume percentage of nanoparticles in several theoretical models. According to the illustration, various higher-order theories and Reddy beam theory are more accurate than Timoshenko beam theory. This difference in prediction arises due to inherent physical restrictions contained within the theory of Timoshenko beam models. The limitations in availability for Timoshenko beam models are separate from the relatively more accurate predictive abilities of the Reddy beam type and other higher-order theories. The theory of Timoshenko beam improves upon of nanostructured composites. More sophisticated higher-order theories like Reddy's and others include the non-local effects and the strain gradient stresses, and an enhanced parabolic classical Euler-Bernoulli theory, in that it includes shear deformations, but it remains insufficient for nearly all physical modeling of the complex multi-scale interactions occurring in the microstructure shear strain distribution across the thickness of a composite beam. The pursuit of accurate stiffness characterization for nanoscale composites necessitates models that faithfully represent both shear deformation and size-dependent effects. Simplified approaches, such as those based on Timoshenko beam theory, are inherently limited in this regime, as they cannot account for the micro-scale interactions that become significant at larger volume fractions of nanoparticles. These models thus yield only a representative stiffness. This work employs a more rigorous higher-order composite theory, which explicitly captures these critical phenomena. The result is a significantly more accurate and trustworthy prediction of non-dimensional frequency, an improvement that is most pronounced under conditions of increasing nanoparticle loading.

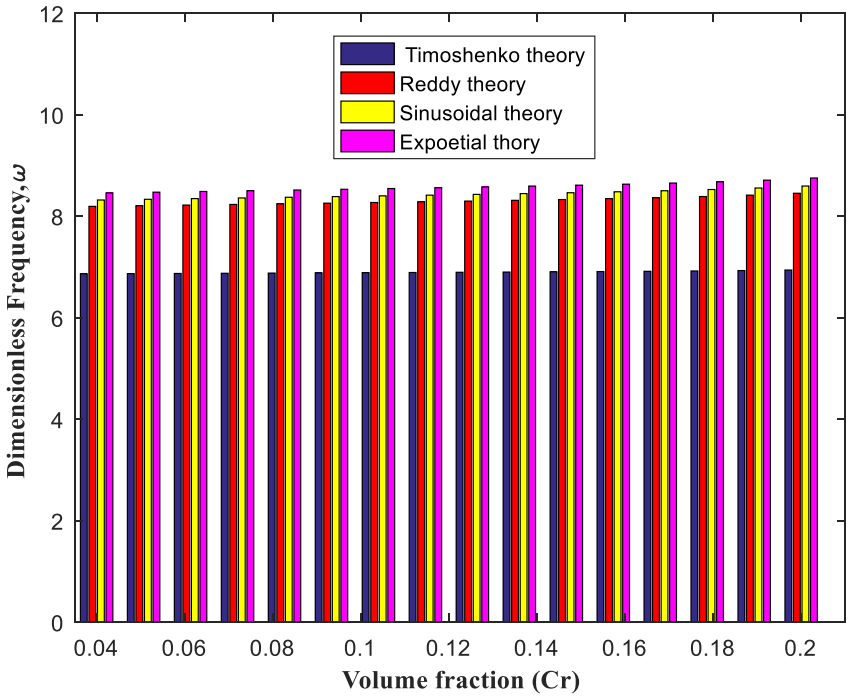


Fig. 16 The bar chart of nanoparticle volume percentage versus non-dimensional frequency for different theories.

The combined effects on the dimensionless frequency of the length-to-thickness ratio are shown in Figure 17. The picture illustrates how dimensionless frequency rises with increasing thickness and falls with increasing length. The two characteristics of the system—stiffness and inertia—can be used to explain this. Because longer structures are generally more flexible, their natural frequency (an inertia-dominated response) will be smaller. In contrast, a structure with more thickness will eventually have a higher natural frequency because of its increasing stiffness. The figure also indicates that the role of thickness has diminished in frequency with longer ratios. In this case, due to the greater flexibility of longer sections, the stiffness of the cross-section does not have as large a change with added thickness.

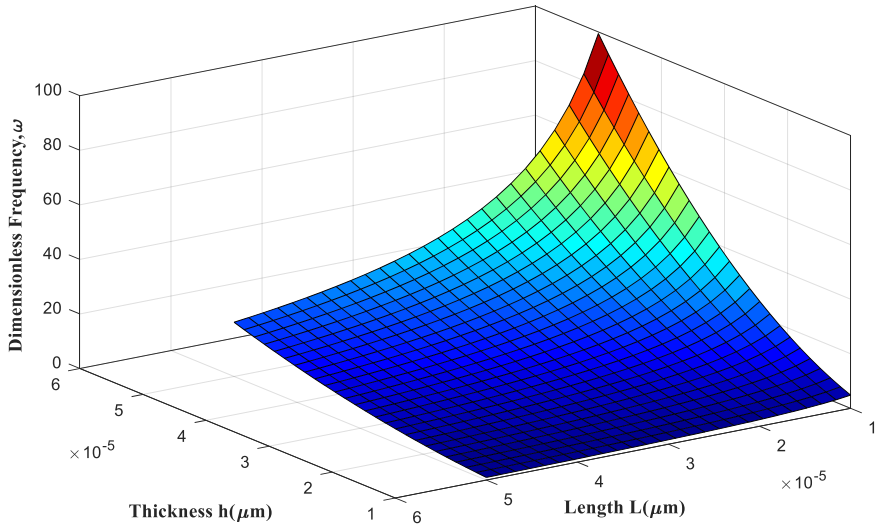


Fig. 17 The simultaneous effect of the microbeam's length and thickness on the dimensionless frequency.

Figure 18 illustrates the combined impact of the thickness to length ratio on the dimensionless frequency. The dimensionless frequency rises with increasing thickness while decreasing with increasing length, as the graphic illustrates. This can be explained in a tangible way. A longer structure tends to also be more flexible, which decreases the natural frequency (inertia-dominated), while a larger thickness improves the structural stiffness, increasing the natural frequency. In addition, the figure indicates that the effect of thickness on the frequency becomes less significant as the length goes to infinity. This is explained by the fact that overall flexibility becomes the most important parameter for very long structures, making the system less susceptible to variations in cross-sectional stiffness (caused by changes in thickness).

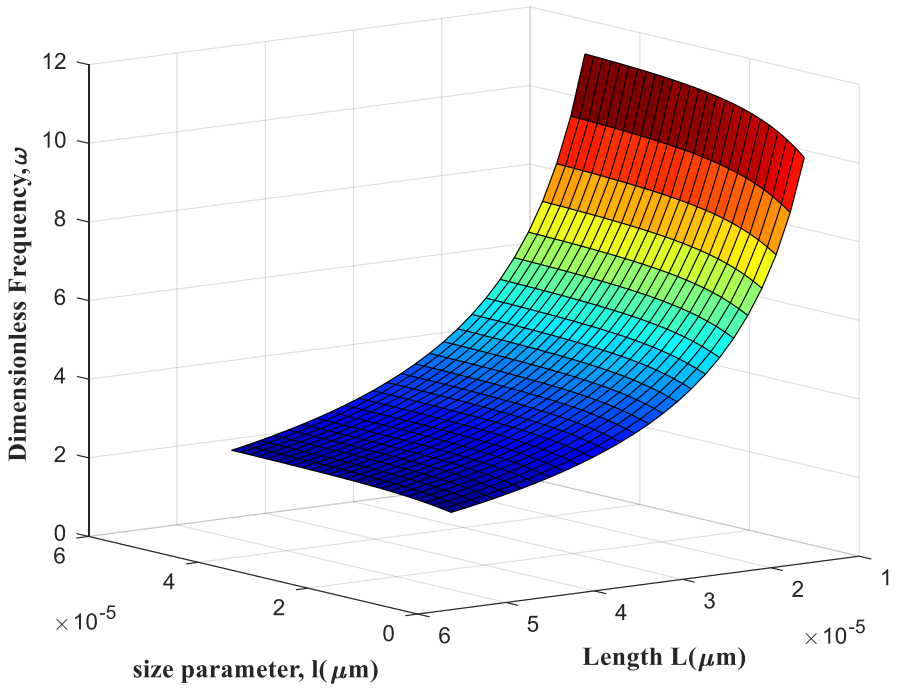


Fig. 18 The effect of the microbeam thickness on the dimensionless frequency for different values of the small-scale coefficient.

Fig. 19 gives the bandgap and acoustic response of the metamaterial microbeam. There is a stopband between 1e7 Hz and 2.63e7 Hz in which there is no propagation of waves. The upper edge of the stopband is taken as the upper dispersion surface when $\beta \to 0$ and the lower dispersion surface, and the bottom edge is also taken as the bottom dispersion surface for $\beta \to \infty$ as:

$$\frac{1}{2}\frac{\sqrt{-2M_2M_3\left(Kg_2M_3+Kg_3M_2+Kg_3M_3\right)-\sqrt{Kg_2^2M_3^2-2Kg_2Kg_3M_2M_3+2Kg_2Kg_3M_3^2+Kg_3^2M_2^2+2Kg_3^2M_2M_3+Kg_3^2M_3^2}}}{M_2M_3i} \tag{85}$$

$$\frac{1}{2}\frac{\sqrt{-2M_2M_3\left(Kg_2M_3+Kg_3M_2+Kg_3M_3\right)+\sqrt{Kg_2^2M_3^2-2Kg_2Kg_3M_2M_3+2Kg_2Kg_3M_3^2+Kg_3^2M_2^2+2Kg_3^2M_2M_3+Kg_3^2M_3^2}}}{M_2M_3i} \tag{86}$$

The plot shows how the frequency (ω) and wave number (α) are correlated; the different branches of dispersion are shown by the purple dashed line and the red solid. A distinct boundary between the two branches is evident, indicating a frequency range where wave propagation is prohibited.

The propagating mode of the lower frequencies is represented by the lower dispersion branch (red line), and the localized or evanescent mode of the resonating microstructure is represented by the upper branch (purple dashed line). The existence of the bandgap indicates that the metamaterial can regulate the transmission of elastic waves, taking advantage of the local resonance effects, which are controlled by the geometry and material properties of the microbeam.

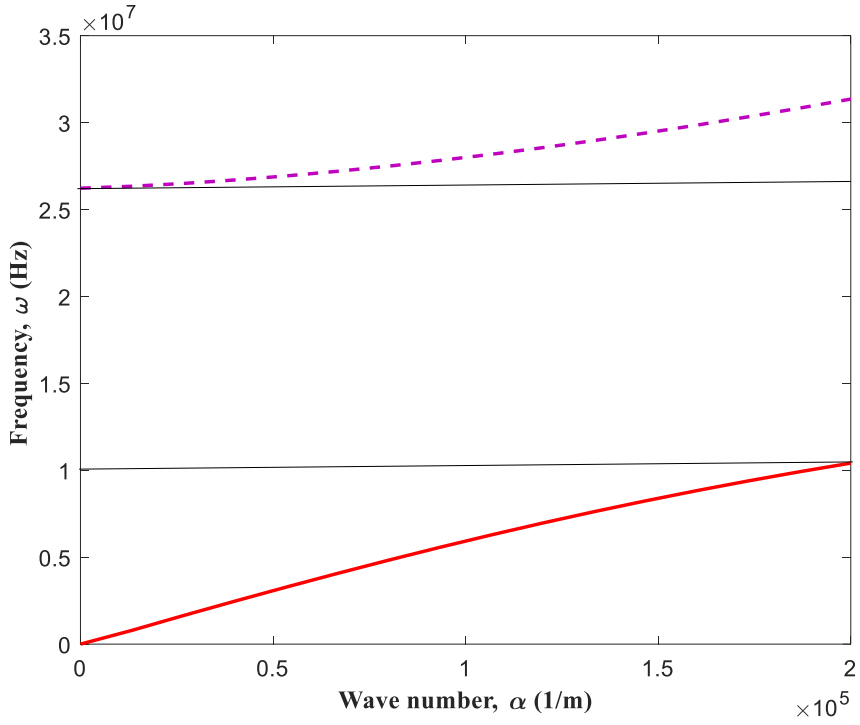


Fig. 19 The bandgap and acoustic response of the metamaterial microbeam.

4-Conclusion

This study has investigated the acoustic response and vibration of FG metamaterial microbeams while accounting for surface effects. CNTs were employed as reinforcements, the Gurtin-Murdoch theory was used to simulate the impacts of surface tension, and the Mori-Tanaka model was used to explain the effects of agglomeration and nanoparticle distribution. The frequency and bandgaps of the microstructure were calculated with the help of analytical techniques. The findings reveal

that the geometry parameters, the FG index, percentage of nanoparticles and agglomeration, and the small-scale parameter have a great impact on the vibration properties of the microbeam. The findings present some informative knowledge as:

- As the microbeam thickness grows between 15 μm and 30 μm, the frequency curve rises by about 82% because of the corresponding increase in bending stiffness.
- The frequency rises by 5.48% as the small-scale coefficient is increased by 15 μm to 30 μm, demonstrating the hardening effect of size-related effects.
- The Timoshenko beam theory has an approximation of between 7.75% underestimation when compared to the higher-order theories in estimating the frequency due to its neglect of nonlocal and strain-gradient effects.
- The frequency is positively influenced by the thickness and the small-scale parameter; the higher the values, the stronger the structure and the higher the total natural frequency.
- The frequency increases with an increase in the volume fraction of the nanoparticles with an increase in the structural rigidity, particularly with the increase in the small-scale parameters.
- Since localized mass clustering and decreased effective stiffness result from nanoparticle agglomeration, frequency is lower than in the theoretical uniform scenario.
- The increase in FGM gradient index leads to the frequency decreasing because the introduction of soft material areas leads to a decrease in the overall bending stiffness of the microbeam.
- The metamaterial's ability to regulate acoustic waves by local resonance is demonstrated by the stopband, which is positioned between 1.0 × 107 Hz and 2.63 × 107 Hz, the bandgap, which is around 1.63 × 10 7 Hz, and the blocking of wave propagation.

Reference

1. Chen, C., et al., Impact dynamics of mechanical metamaterials: A short review and perspective. Forces in Mechanics, 2025: p. 100335.
2. Zhang, H., et al., Dynamic mechanical behavior of sponge-inspired metamaterials with enhanced energy absorption and tunable Poisson's ratio. Construction and Building Materials, 2025. **496**: p. 143822.
3. Li, S., et al., Metamaterial structures incorporating configuration-dependent surface and nonlocal effects. Composite Structures, 2025. **372**: p. 119560.
4. Han, D., et al., Utilizing partially-curved-beam to improve stress response and energy absorption performance of auxetic lattice metamaterials. Thin-Walled Structures, 2025. **217**: p. 113896.
5. Guo, X.L. and B.H. Sun, Reinforced design and temperature-varying compressive performance investigation of aperiodic honeycomb metamaterials. Composite Structures, 2025. **372**: p. 119541.
6. Zhao, L., et al., A viscoelastic metamaterial beam for integrated vibration isolation and energy harvesting. Applied Mathematics and Mechanics, 2024. **45**(7): p. 1243–1260.
7. Chen, X., et al., Broadband Vibration Reduction of Single-Beam Honeycomb Metamaterial with Tunable Bandgap Characteristics. Journal of Vibration Engineering & Technologies, 2025. **13**(1): p. 28.
8. Wu, Q., et al., Influences of inherent geometrical nonlinearity of high-static-low-dynamic-stiffness resonator on flexural wave attenuation performance of metamaterial beam. Nonlinear Dynamics, 2024. **112**(10): p. 7831–7845.
9. Gao, Y. and L. Wang, An active tunable piezoelectric metamaterial beam for broadband vibration suppression by optimization. Acta Mechanica Sinica, 2023. **40**(3): p. 523235.
10. Guo, D., et al., Numerical and experimental investigations on flexural vibration characteristics of metamaterial beam with carbon fiber-reinforced polymers. Mechanics of Advanced Materials and Structures, 2024. **31**(16): p. 3690–3699.
11. Pancella, C. and F. D'Annibale, A Timoshenko-like equivalent beam model for the static analysis of a chiral metamaterial. Continuum Mechanics and Thermodynamics, 2025. **37**(4): p. 59.
12. Failla, G., A. Burlon, and A.F. Russillo, A novel metamaterial multiple beam structure with internal local resonance. Acta Mechanica, 2024. **235**(9): p. 5885–5903.
13. Guo, Z., et al., Ultra-Low-Frequency Vibration Attenuation Characteristics of Multi-Span Metamaterial Dual-Beam Structures. Mechanics of Solids, 2024. **59**(1): p. 431–444.
14. Yu, M., et al., Robust nonlinear elastic metamaterial enabled by collision damping. Mechanics of Advanced Materials and Structures, 2024. **31**(16): p. 3630–3637.
15. Furjan, M., R. Kolahchi, and M. Yaylacı, Energy harvesting capabilities and bandgaps of locally resonant piezoelectric metamaterial panels with self-extraction synchronized circuit. Applied Mathematical Modelling, 2025. **141**: p. 115934.
16. Naseer, H., et al., Effect of flexibility on energy harvesting performance of semi-active flapping foil under non-sinusoidal pitching motion. Ocean Engineering, 2025. **341**: p. 122462.
17. Chen, Z., et al., Tunable in-plane mechanical properties of the novel re-entrant auxetic structure with sinusoidal inclusion. Results in Engineering, 2025. **28**: p. 107546.

18. Xiao, L., et al., Friction performance optimization based on sinusoidal microtexture-DLC coating coupling: Effect of circular frequency on reciprocating friction mechanism. Diamond and Related Materials, 2025. **159**: p. 112719.
19. Kumar, S. and S.K. Verma, Three-dimensional simulation and experimental validation of solar air heater having sinusoidal rib. Energy Sources, Part A: Recovery, Utilization, and Environmental Effects, 2024. **46**(1): p. 16865–16883.
20. Xing, X. and J. Liu, Adaptive Vibration Control of a Class of Telescopic Timoshenko Beams with Uncertain Payloads and Output Constraints based on Partial Differential Equation Models. Communications in Nonlinear Science and Numerical Simulation, 2025: p. 109378.
21. Rodríguez-Cruz, W., et al., Correction in the continuity conditions for beams with structure governed by the Timoshenko–Ehrenfest equation. Wave Motion, 2025. **139**: p. 103582.
22. Ai, Z.Y., et al., Performance analysis of Timoshenko beams on transversely isotropic porous subgrade due to moving loads considering thermal effects. Soil Dynamics and Earthquake Engineering, 2025. **193**: p. 109286.
23. Wu, S. and M. Ling, A dynamic Timoshenko beam constraint model for use in compliant mechanisms with intermediate deformation ranges. Precision Engineering, 2025. **94**: p. 447–460.
24. Ouzizi, A., F. Abdoun, and L. Azrar, Nonlinear dynamics of Timoshenko beams on nonlinear fractional viscoelastic Pasternak foundation under a moving mass. Engineering Structures, 2025. **339**: p. 120543.
25. Schoeftner, J., Vibrations of a piezoelectric Timoshenko beam with resistive-inductive electrodes. Meccanica, 2025.
26. Brethee, K.F. and M.J. Awad, Vibration Analysis of Timoshenko Beam Subjected to a Moving Mass and Suffering from an Open Crack. Russian Journal of Nondestructive Testing, 2025. **61**(4): p. 490–503.
27. Bazoune, A. and M.U. Khan, Dynamic Modeling and Analysis of Centrifugally Stiffened Proportionally Damped Timoshenko Beam. Journal of Vibration Engineering & Technologies, 2024. **12**(4): p. 6101–6119.
28. Nascimento, F.A.F., et al., Decay rates for Timoshenko beam system with suspenders and arbitrary nonlinear localized damping. Acta Mechanica, 2025. **236**(3): p. 1487–1508.
29. C. Chu, M.S.H.A.-F., R. Kolahchi, Energy harvesting and dynamic response of SMA nano conical panels with nanocomposite piezoelectric patch under moving load. Engineering Structures, 2023. **292**: p. 116538.
30. Furjan, M., et al., Energy harvesting and forced vibration of flexoelectric hydrogel-based triboelectric spherical cap microgenerators. Acta Mechanica, 2025. **236**(3): p. 1719–1759.
31. Wanji, C., W. Chen, and K.Y. Sze, A model of composite laminated Reddy beam based on a modified couple-stress theory. Composite Structures, 2012. **94**(8): p. 2599–2609.
32. Wan, P.H., et al., Application of DQHFEM for free and forced vibration, energy absorption, and post-buckling analysis of a hybrid nanocomposite viscoelastic rhombic plate assuming CNTs' waviness and agglomeration. Mechanical Systems and Signal Processing, 2023. **189**: p. 110064.
33. Al-Furjan, M.S.H., et al., The Mechanics of Smart Nanocomposite Sandwich Structures. 2023, Cambridge Scholars Publishing.

34. Şimşek, M. and J.N. Reddy, Bending and vibration of functionally graded microbeams using a new higher order beam theory and the modified couple stress theory. International Journal of Engineering Science, 2013. **64**: p. 37–53.

Appendix A

$$k_{11} = A_{11}\beta^2 \tag{A1}$$

$$k_{12} = -B_{11}\beta^3 + B_{33}\left(\frac{\tau_s\beta^3}{h}\right) \tag{A2}$$

$$k_{13} = -E_{11}\beta^2 \tag{A3}$$

$$k_{14} = 0 \tag{A4}$$

$$k_{15} = 0 \tag{A5}$$

$$k_{21} = -B_{11}\beta^3 \tag{A6}$$

$$k_{22} = D_{11}\beta^4 + D_{33}\left(\tau_s\beta^4\right) + A_{11}\beta^4 l^2 \tag{A7}$$

$$k_{23} = -F_{11}\beta^3 - \frac{D_{55}\left(l^2\beta^3\right)}{2} \tag{A8}$$

$$k_{24} = 0 \tag{A9}$$

$$k_{25} = 0 \tag{A10}$$

$$k_{31} = E_{11}\beta^2 \tag{A11}$$

$$k_{32} = -F_{11}\beta^3 + F_{33}\left(\tau_s\beta^3\right) - \frac{D_{55}l^2\beta^3}{2} \tag{A12}$$

$$k_{33} = H_{11}\beta^2 + \frac{B_{55}l^2\beta^2}{4} + \frac{E_{55}l^2}{4} + B_{55} \tag{A13}$$

$$k_{34} = 0 \tag{A14}$$

$$k_{35} = 0 \tag{A15}$$

$$k_{41} = 0 \tag{A16}$$

$$k_{42} = -Kg_2 \tag{A17}$$

$$k_{43} = 0 \tag{A18}$$

$$k_{44} = Kg_2 + Kg_3 \tag{A19}$$

$$k_{45} = -Kg_3 \tag{A20}$$

$$K_{51} = 0 \tag{A21}$$

$$K_{52} = 0 \tag{A22}$$

$$K_{53} = 0 \tag{A23}$$

$$K_{54} - Kg_3 \tag{A24}$$

$$K_{55} = Kg_3 \tag{A25}$$

$$m_{11} = I_0 \Omega^2 i^2 \tag{A26}$$

$$m_{12} = -B_{33}\left(\frac{\Omega^2 \beta^2 i^2 \rho_s}{h}\right) + I_1 i^2 \beta \Omega^2 \tag{A27}$$

$$m_{13} = -I_3 i^2 \Omega^2 \tag{A28}$$

$$m_{14} = 0 \tag{A29}$$

$$m_{15} = 0 \tag{A30}$$

$$m_{21} = I_1 \Omega^2 \beta^2 i^2 \tag{A31}$$

$$m_{22} = -D_{33}\Omega^2 \beta^2 i^2 \rho_s - I_0 \Omega^2 i^2 - I_2 \Omega^2 \beta^2 i^2 \tag{A32}$$

$$m_{23} = I_4 \Omega^2 \beta i^2 \tag{A33}$$

$$m_{24} = 0 \tag{A34}$$

$$m_{25} = 0 \tag{A35}$$

$$m_{31} = -I_3 \Omega^2 i^2 \tag{A36}$$

$$m_{32} = -F_{33}\Omega^2 \beta i^2 \rho_s + I_4 \Omega^2 \beta i^2 \tag{A37}$$

$$m_{33} = -I_5\Omega^2 i^2 \tag{A38}$$

$$m_{34} = 0 \tag{A39}$$

$$m_{35} = 0 \tag{A40}$$

$$m_{41} = 0 \tag{A41}$$

$$m_{42} = 0 \tag{A42}$$

$$m_{43} = 0 \tag{A43}$$

$$m_{44} = M_2\Omega^2 i^2 \tag{A44}$$

$$m_{45} = 0 \tag{A45}$$

$$m_{51} = 0 \tag{A46}$$

$$m_{52} = 0 \tag{A47}$$

$$m_{53} = 0 \tag{A48}$$

$$m_{54} = 0 \tag{A49}$$

$$m_{55} = M_3\Omega^2 i^2 \tag{A50}$$